

Citation for the published version:

Tao, Z., Cheng, Z., Zhu, J., Lin, D., & Wu, H. (2018). Large eddy simulation of supercritical heat transfer to hydrocarbon fuel. *International Journal of Heat and Mass Transfer*, 1251-1263. [121]. DOI: 10.1016/j.ijheatmasstransfer.2018.01.089

Document Version: Accepted Version

This manuscript is made available under the CC-BY-NC-ND license
<https://creativecommons.org/licenses/by-nc-nd/4.0/>

Link to the final published version available at the publisher:

<https://doi.org/10.1016/j.ijheatmasstransfer.2018.01.089>

General rights

Copyright© and Moral Rights for the publications made accessible on this site are retained by the individual authors and/or other copyright owners.

Please check the manuscript for details of any other licences that may have been applied and it is a condition of accessing publications that users recognise and abide by the legal requirements associated with these rights. You may not engage in further distribution of the material for any profitmaking activities or any commercial gain. You may freely distribute both the url (<http://uhra.herts.ac.uk/>) and the content of this paper for research or private study, educational, or not-for-profit purposes without prior permission or charge.

Take down policy

If you believe that this document breaches copyright please contact us providing details, any such items will be temporarily removed from the repository pending investigation.

Enquiries

Please contact University of Hertfordshire Research & Scholarly Communications for any enquiries at rsc@herts.ac.uk

Large eddy simulation of supercritical heat transfer to hydrocarbon fuel

Zhi Tao^a, Zeyuan Cheng^a, Jianqin Zhu^{a,*}, Dasen Lin^a, Hongwei Wu^{b,**}

^aNational Key Laboratory of Science and Technology on Aero-Engine Aero-thermodynamics,
School of Energy and Power Engineering, Beihang University, Beijing 100191, China

^bSchool of Engineering and Technology, University of Hertfordshire, Hatfield, AL10 9AB, United
Kingdom

* Corresponding author. Email: zhuqianbuaa@sina.com Tel. +86(010)82339181

** Corresponding author. Email: h.wu6@herts.ac.uk Tel. +44(0) 1707 284265;
Fax. +44(0) 1707 285086

Abstract

In this article, a large eddy simulation (LES) method for the heat transfer of the hydrocarbon fuel flowing through the uniformly heated miniature round pipe at supercritical pressure has been formulated and validated. The four species surrogate model was used to simulate the real thermophysical properties of the fuel. Validation of the developed LES model was carried out through comparisons of the wall temperature and pressure drop with available experimental data and other turbulence model results. Results show that the LES gave the best prediction. Further calculations based on the proposed LES for three cases including subcritical, transcritical and supercritical temperature ranges were numerically investigated in a systematic manner. It was found that the entrance effect occurred among the subcritical, transcritical and supercritical temperature cases that caused by the developing thermal boundary layer. The significant variation of the thermophysical properties near the pseudo-critical temperature would weaken the heat transfer in the transcritical case where the velocity fluctuation affected more on turbulent heat transfer than the temperature fluctuation did.

Keywords: Large eddy simulation; Hydrocarbon fuel; Supercritical; Heat transfer; Turbulence model.

Nomenclature		
C_p	Specific heat at constant pressure	J/(Kg·K)
d	Diameter of the tube	mm
g	<i>Gravitational acceleration</i>	m/s^2
G	Filter function	
h	Heat transfer coefficient	$h_f = q_w / (T_w - T_f)$
H	Enthalpy	J/kg
k	Turbulent kinetic energy	m^2/s^2
m	Mass flow rate	g/s
P	Pressure	MPa
Pr	Molecular Prandtl number	
Pr _{SRS}	Subgrid Prandtl number	
q	Wall heat flux	kW/m ²
T	Temperature	K
u	Velocity	m/s
x	Axial direction	mm
y^+	Wall dimensionless distance	
Greek symbols		
μ	Molecular viscosity	$\mu Pa \cdot s$
μ_{SRS}	Subgrid viscosity	$\mu Pa \cdot s$
ρ	Density	kg/m ³
κ	Thermal conductivity	W/(m·K)
ν	Turbulence frequency	s ⁻¹
τ	Subgrid stress	Pa
σ	Viscosity stress	
Subscripts/over-bars		
b	Bulk	
f	forced	
in	Inlet	
out	Outlet	
Pc	Pseudo-critical	
w	Wall	
'-'	Over-bar used for filter	

1. Introduction

The critical phenomena have been long recognized for nearly two hundred years and continue to make significant and extensive applications in the modern society [1]. In the 1960s and 1970s, the supercritical water steam was selected as the power source to drive the steam turbine in the regular fossil fuel power plants due to its higher energy conversion efficiency. Subsequently, after several decades of silence, the development of a new type of supercritical water reactor (SCWR) has again driven the interest for the supercritical water in around 2000 [2]. Besides, the supercritical hydrogen and supercritical aviation kerosene have played crucial roles in air-conditioners [3] and advanced aircraft engines [4].

Recently, with the development of hypersonic vehicle, the scramjet engine has been a hotspot due to its hypersonic speed which may lead to a very severe thermal management problem [5]. It is a common approach to resolve the problem using regenerative cooling technology. During the cooling process, the hydrocarbon fuel is driven under supercritical pressure to flow through the cooling channel near combustor and absorbs heat from high-temperature combustor by physical and chemical heat sinks, then it is injected from the nozzles into the combustor to accomplish the energy transportation [6]. Therefore, the heat trapping ability of supercritical hydrocarbon fuel has an important influence on the operating performance of the regenerative cooling system.

To achieve both the design and application of the supercritical equipment, the characteristics of the thermophysical property and turbulent heat transfer of the supercritical fluids have been widely investigated [7-8]. At supercritical pressure, with temperature increasing, a peak of the specific heat occurs at the point called pseudo-critical temperature, in the vicinity of which, the density, viscosity and thermal conductivity undergo significant changes. It is recognized that the

significant variations of the thermophysical properties with temperature at supercritical pressure may lead to the heat transfer enhancement or heat transfer deterioration (HTD), depending on the heat flux to mass flux ratio at certain inlet temperature [9]. However, owing to the limitation of the measurement instrument, the obtained data from the experiments might be focused mainly on the wall temperature and flow resistance loss [10], while it is scarce or difficult to obtain in regard to the data demonstrating the detailed flow field quantity like the velocity and turbulence, which could be very helpful to penetrate into the nature of peculiar turbulent heat transfer under supercritical pressure.

Nowadays, the rapid development of the computer capacity makes the computational fluid dynamics (CFD) more accessible to assist the experiment method as the comprehensive analysis tool. There are mainly three kinds of CFD methods based the simulated turbulence fine level [11]. The Reynolds-averaged Navier-stokes (RANS) method is mostly used to simulate the supercritical flow and heat transfer in which turbulence models play a key role [12]. He et al. [13] performed numerical simulations of turbulent mixed convection heat transfer experiments with supercritical carbon dioxide flowing in a uniformly heated vertical tube. They found that most of the low Reynolds k - ϵ turbulence model could reproduce qualitatively supercritical heat transfer with obvious buoyancy, however, the performance of turbulence models varied significantly from one to another in terms of the HTD onset. Compared with the two equation turbulence model, the four-equation model and Reynolds-stress model show the better performance in predicting the supercritical heat transfer deterioration but still over predicted wall temperature and heat transfer deterioration onset [14].

The direct numerical simulation (DNS) method is adopted to resolve the turbulent motion in

all scales [15]. However, very high quality mesh is required to capture the tiny vortex and fluctuation motion existing in the supercritical turbulent flow. Bae et al. [16,17] made significant achievements in the supercritical DNS simulation of carbon dioxide in a vertical heated round tube. The detailed turbulent statistics data was obtained in order to thoroughly understand the mechanism of the heat transfer deterioration in upward flow, meanwhile, it served as the reference library for the comparison of RANS computations [18].

Since high cost of the DNS method in the computer memory, processor and time consumption, the high Reynolds flow and large geometry flow are difficult to be simulated by DNS method. As such, the large eddy simulation method (LES) emerges due to its moderate computer cost and the ability to resolve the large eddy [19]. Wang et al. [20] carried out the LES computations for the turbulent flow of supercritical carbon dioxide flowing in a uniformly heated tube. A specific section was assigned as an inflow generator to construct the time dependent subsonic inflow boundary condition and a good agreement with the DNS results from Bae et al.

[21] at relatively low Reynolds number was achieved. Niceno and Sharabi [21] conducted the study of turbulent heat transfer LES of supercritical water flowing in an externally heated pipe for both the downward and upward flow cases. It showed that the LES results could observe the wall temperature trend from the experiments both qualitatively and quantitatively. The buoyancy production of turbulence was larger compared to the total production of turbulence in the upward flow but smaller in the downward flow.

Although several studies regarding supercritical injection of hydrocarbon fuel using LES have been already carried out by now [22], but quite few studies have been conducted in the use of LES to investigate the hydrocarbon fuel flowing at supercritical pressure in the cooling process.

From the mechanism research's point of view, the purpose of the present study is to perform a systematic evaluation of the current computational capability of LES to capture the turbulent flow and heat transfer of the supercritical hydrocarbon fuel flowing in the heated miniature round tube. In order to assess the proposed LES model as an analysis tool for carrying out more studies to further elucidate the pertinent physical phenomena involved in the study, the computed results with LES are compared with available experimental data and other turbulence model results. Moreover, three cases including subcritical and supercritical inlet temperatures are simulated and the effect of the variation of the thermophysical properties with temperature on turbulent heat transfer is analyzed in detail.

2. Mathematical model and numerical analysis

In this section, the fluid properties, computational model and mesh, governing equations, boundary conditions, RANS models and solution methods are addressed below.

2.1. Fluid properties

In the present study, the working fluid used is the typical hydrocarbon fuel, aviation kerosene RP-3 (Rocket Propellant), which is composed of tens of thousands of different types of components, including alkane, olefin and aromatic hydrocarbon, etc. Four species surrogate model, consisting of 19.1% n-decane, 36.5% n-dodecane, 29.9% n-butylbenzene and 14.5% methyl-cyclohexane, is used to simulate the real thermophysical properties of RP-3 [23]. The self-developed thermophysical properties computation code can compute the density, viscosity, thermal conductivity and specific heat at the given pressure and temperature. Variations of four kinds of properties of the four-species surrogate model with temperature at 5 MPa are shown in Fig. 1. It can be seen that all the thermophysical properties undergo a dramatic variation with the

increase of temperature at constant pressure in the vicinity of the pseudo-critical temperature in which the specific heat is at maximum. The detailed computational method and further comparison and validation with NIST (the National Institute of Standards and Technology) thermophysical properties of hydrocarbon mixtures database [24] have been introduced in our previous studies [17,25]. The calculated critical temperature and critical pressure are 643.5 K and 2.43 MPa, respectively, while the corresponding values obtained from the experiments are 645.04K and 2.33MPa [26]. Good agreements between the calculated values and the measured values confirm the accuracy of the thermophysical property model. It has been verified that the thermophysical properties model of RP-3 is reliable for LES computations.

2.2. Computational model and mesh

The computational model is a long straight round tube, with length of 350 mm and diameter of 1.8 mm. Fig. 2 gives the schematic diagram of the computational model. A 50 mm long adiabatic section (*C* in Fig. 2) is set up at the beginning of the tube and the rest of the tube (*D* in Fig. 2) is uniformly heated to simulate the heat from high temperature components (*E* in Fig. 2). The inflow (*A* in Fig. 2) enters the physical model through the inlet (*B* in Fig. 2) of the tube, and the outflow (*G* in Fig. 2) exits by the outlet (*F* in Fig. 2).

A 3D structured mesh is used for discretizing the computational fluid domain, covering the adiabatic and heated sections. LES has a rigorous requirement for grid resolution, especially in the heated section and the region near wall. A mesh independence study was conducted to identify an appropriate mesh density for the aimed calculations, as illustrated in Fig. 3. The detailed information on the experimental results [31] in Fig. 3 can be seen in Section 3. In the current work, a 3,564,684 cells of mesh was selected in which the distance between two adjacent nodes

grows by a factor of 1.05 with the increase of the distance from the inner wall in the fluid domain. The first node close to the walls has $y^+ < 0.3$ in all runs, meanwhile, 8 layers of grid points exist in the viscous sublayer where $y^+ < 6$. Table 1 illustrates the grid resolution in the fluid domain. It gives the non-dimensional size of the mesh cell in different directions and y^+ is the non-dimensional height of the first-layer grid off the wall. These values in Table 1 are within the recommended range of $y^+ < 1$, $\Delta x^+ = 50 - 100$ and $\Delta z^+ = 10 - 20$ for the wall-resolving LES [27]. In addition, the mesh of the computational model is shown in Fig. 4, including the side view, streamwise view and the whole view of mesh.

2.3. Governing equations

In the present study, the governing equations employed are obtained via filtering the instantaneous equations, including mass conservation, momentum conservation and energy conservation.

Continuity equation:

$$\frac{\partial \rho}{\partial t} + \frac{\partial(\rho \bar{u}_i)}{\partial x_i} = 0 \quad (1)$$

where ρ is the density, \bar{u}_i is the velocity tensor, x_i is the coordinate tensor and t is the time.

Momentum equation:

$$\frac{\partial}{\partial t}(\rho \bar{u}_i) + \frac{\partial}{\partial x_j}(\rho \bar{u}_i \bar{u}_j) = \rho \bar{g}_i - \frac{\partial \bar{P}}{\partial x_i} + \frac{\partial \tau_{ij}}{\partial x_j} + \frac{\partial(\sigma_{ij})}{\partial x_j} \quad (2)$$

where σ_{ij} is the stress tensor due to the molecular viscosity, P is the pressure and τ_{ij} is the subgrid stress (SRS).

Energy equation:

$$\frac{\partial \rho \bar{H}}{\partial t} + \frac{\partial}{\partial x_i}(\rho \bar{u}_i \bar{H}) = \bar{u}_i \frac{\partial \bar{P}}{\partial x_i} + \frac{\partial}{\partial x_i} \left(\lambda \frac{\partial \bar{T}}{\partial x_i} \right) + \frac{\partial}{\partial x_j}(\rho \bar{u}_j \bar{H} - \rho \overline{u_j H}) \quad (3)$$

where \bar{H} is the enthalpy and λ is the thermal conductivity.

The SGS term is divided into the isotropic and deviatoric parts:

$$\tau_{ij} = \underbrace{\tau_{ij} - \frac{1}{3} \tau_{kk} \delta_{ij}}_{\text{deviatoric}} + \underbrace{\frac{1}{3} \tau_{kk} \delta_{ij}}_{\text{isotropic}} \quad (4)$$

In the current study, the term τ_{kk} can be ignored for the incompressible flows as the pressure drop

along the tube is very small compared with the absolute pressure and the thermophysical properties vary with temperature. Also it can be neglected because of the small flow Mach number (less than 0.01 along the whole tube).

The deviatoric part in SGS term can be modelled by eddy diffusion type as shown below:

$$\underbrace{\tau_{ij} - \frac{1}{3}\tau_{kk}\delta_{ij}}_{\text{deviatoric}} = -2\mu_{SGS}\left(S_{ij} - \frac{1}{3}S_{kk}\delta_{ij}\right) \quad (5)$$

where S_{ij} is the strain rate tensor, μ_{SGS} is the subgrid viscosity and δ_{ij} is the kronecker symbol.

The Smagorinsky-Lilly model is used to model the SGS viscosity:

$$\mu_{SGS} = \rho L_m^2 \left(2\bar{S}_{ij}\bar{S}_{ij}\right)^{1/2} \quad (6)$$

where L_m is the mixing length for SGS computed by the expression shown below:

$$L_m = C_s \Delta \quad (7)$$

where C_s is the Smagorinsky coefficient and Δ is the subgrid scale computed by:

$$\Delta = V^{1/3} \quad (8)$$

According to the -5/3 Kolmogorov pow law of the turbulent kinetic energy spectrum, the Smagorinsky coefficient is obtained:

$$C_s = \frac{1}{\pi} \left(\frac{2}{3C_k} \right)^{3/4} \quad (9)$$

where C_k is the Kolmogorov constant, 1.4 [1].

In the very vicinity of the wall, the SGS is equal to zero due to the zero turbulent fluctuation, therefore the complementary rule is set that near the wall $L_m = \kappa l$ in which κ is the von Karman constant of 0.41 and l is the distance from the wall.

In the following analysis, the convective heat transfer coefficient is calculated by the expression below:

$$h = \frac{q_w}{T_w - T_b} \quad (10)$$

where q_w is the wall heat flux, T_w is the wall temperature and T_b is the bulk temperature.

The definition of the non-dimensional distance from the inlet of the heating section is given below:

$$x/d = (X - l)/d \quad (11)$$

where x and X are the distance from the inlet of the whole pipe and from the inlet of the heating section, respectively. d is the tube diameter and l is the length of the adiabatic section.

In current study, d is taken as 0.0018 and l is 0.05.

2.4 Boundary conditions

To consider the variable property flow at supercritical pressure, the velocity-inlet type and pressure-outlet type were chosen for the inlet and outlet boundary conditions, respectively. The constant heat flux boundary condition was imposed on the uniformly-heated section, meanwhile the heat flux was set to zero on the adiabatic tube wall. In the current study, the pressure is 5 MPa and the inlet mass rate is 3 g/s for all three cases. For case 1, the imposed heat flux is 442 kW/m² and the inlet temperature is 571.23 K. For case 2, the imposed heat flux is 260 kW/m² and the inlet temperature is 673.15 K. For case 3, the imposed heat flux is 371 kW/m² and the inlet temperature

is 573.15 K.

2.5 RANS models

RANS turbulence models introduced in this section are used as reference models, and the aim of this paper is to select the best candidate for the prediction among the LES and the mostly used two-equation turbulence models. Two-equation turbulence models are taken to be the most basic of the ‘complete’ turbulence models in which the transport equations of the turbulent kinetic (k) and its dissipation rate (ϵ) are used independently to simulate the velocity field and capture flows affected by variable length scales. In the present study, two turbulence models we chose were the LS low-Reynolds k - ϵ model and the SST k - ω turbulence model. It was found that the SST k - ω model and LS low-Reynolds k - ϵ model performed well in predicting heat transfer enhancement and heat transfer deterioration of the hydrocarbons under supercritical pressure among all the turbulence models used in our previous study [30].

In the current study, the mesh used for RANS models is different from that for LES, and the typical grid independent studies for two RANS models are given in Fig. 5. u and h are the velocity magnitude and the heat transfer coefficient at a certain point, respectively. As the number of cells reaches to a certain number, the change rate of the monitored quantities is less than 1%, implying that the grid independent solution is achieved. The typical numbers of the optimal mesh of grids for LS k - ϵ and SST k - ω models are 1663637 and 1234950, respectively. The first node close to the wall has $y^+ < 1$ in all cases, in order to compute from the viscous sub-layer.

2.3. Solution methods

All simulations for the present work were solved with ANSYS Fluent commercial software and ran on a cluster of 128 processors with a memory of 16384 MB. The pressure-based

segregated algorithm is used to solve the discretization governing equations. The Green-Gauss cell-based gradient evaluation method is applied for modelling the gradient of the convection and diffusion terms in the flow conservation equation and the standard scheme is used to interpolate the pressure values at the face. The bounded central differencing method is used for the momentum equation and energy equation. The bounded second order implicit method is selected to set time-dependent solution formulations. The absolute convergence criterion of residual for all of the governing equations is set to be less than 10^{-6} [29].

The inlet condition is the key to carry out the LES computations, and the accurate LES computation needs a real turbulence fluctuation profile. Kondo et al. [30] studied the decay of the isotropic turbulence by the random fluctuation generated by Fourier synthesis using LES method and the computation results agreed well with the experiments. In the current study, prior to the aimed LES computation, the steady RANS computation is accomplished for each case to provide with the realistic initial field for LES. A mesh screen located at the beginning of the tube is used to generate the LES inlet perturbation and the vortex method is used to add a perturbation on a specified mean velocity profile via a fluctuating vorticity field.

When performing the time-dependent calculations, the fixed time step is selected. To accurately depict the recognizable vortex motion, the Courant-Friedrich-Levy (CFL) principle is used to determine the time step size Δt :

$$\frac{\Delta t \cdot u_s}{l_s} \leq 0.8 \quad (12)$$

where u_s is the velocity scale, taken as the inlet axial velocity, and l_s is the mesh element length scale. The time step size used in the present study is $2 \times 10^{-5} s$. After the flow becomes statistically steady, the simulated 0.6 s physical time, corresponding to 30,000 time steps, is used

for data sampling and statistical averaging for the analysis below.

3. Results and discussion

In the current study, the LES computations simulated the experimental work conducted by Zhang et al. [31], in their study, the characteristics of the local convective heat transfer of supercritical RP-3 flowing in a vertical round tube were investigated. For the purpose of brevity, the details of the experimental work will not be described here.

The uniformly heated section was implemented by the electric heating tube method, and the hydrocarbon fuel was boosted to the supercritical pressure by high pressure liquid plunger pump. The inlet temperature (T_{in}), operating pressure (P) and inlet mass flow rate (m) were measured respectively. Both subcritical and supercritical inlet temperature are considered in order to cover the broad flow conditions. The simulated experimental conditions have been given in Section 2.4.

3.1. Model validation

Prior to conducting the aimed computations, it is necessary to validate the computational model and the developed code. It is well known that in the RANS method all the turbulence on the grid scale is modeled. In contrast, in the LES approach only the subgrid scale turbulence is modeled while all the turbulence on the grid scale is resolved. The comparisons between the calculated wall temperatures by LES and RANS including SST $k-\omega$ model and LS $k-\varepsilon$ model as well as the experimental data [31] are demonstrated in Fig. 6. It can be seen clearly that the LES gives the best prediction in all the test case conditions. The similar results that the poor performance in predicting supercritical heat transfer by two-equation model can be seen in the previous study by He et al. [23]. It was found that the damping function of the turbulence model might not respond well to the local condition where the thermophysical property varies sharply,

especially near the wall. Besides, the poor prediction of the heat transfer is partly attributed to the inability of the turbulence models in reproducing turbulent kinetic energy.

At supercritical pressure, the variation of the thermophysical property has an important influence on the flow resistance characteristics. Table 2 gives the comparisons of the relative errors of total pressure drops along tube length computed by various models for three cases. In Table 2, the computational results of the LES and RANS under-predict the total pressure drops in the experiments [31]. Relatively, the LES method gives the better results, showing the advantage of more expensive computational method. It is pointed out that the larger value of the relative error on the total pressure drop may be caused by the local flow resistance in the pipe joint which is ignored in the simulation.

To further study the difference between LES and RANS results, the comparison of the calculated UV Reynolds-stress at $x/d = 20$ by different models is shown in Fig. 7. In the current work, U , V and W represent the velocities along X , Y and Z directions, respectively. y and R are the distance from the centerline of the tube along the radial direction and the tube radius, respectively. It is clearly observed that as moving away from the centerline, the Reynolds stress gradually increases. The Reynolds stress is zero at wall and the peak of the Reynolds stress occurs near the wall. The variation of UV Reynolds-stress by SST $k-\omega$ model is very similar as that by LS $k-\epsilon$ model, except for the larger value of the Reynolds stress meaning the larger turbulent transport of energy, hence resulting in the lower wall temperature (shown in Fig. 6). For LES results $x/d = 20$ corresponds to the location where the wall temperature increases dramatically (seen in Fig. 6) and the variation of the thermophysical property has significant effect on the distribution of the Reynolds stress. For RANS methods, it is difficult to capture the effect of the

large eddy on the Reynolds stress and the turbulence model might not respond well to the variable property case at supercritical pressure condition, especially near the wall where the large eddy is intensely disturbed, which might result in that the location of the peak of the Reynolds stress by RANS is closer to the wall than that by LES.

According to the above analysis, LES method is verified to have capacity to be a simulation tool to carry out the comprehensive investigation of the effect of variable property at supercritical pressure condition.

3.2. Wall temperature and detailed fields

3.2.1. Case 1: Transcritical temperature case

Fig. 8 illustrates the variations of the wall temperature, fluid bulk temperature and corresponding heat transfer coefficient with the non-dimensional distance by LES for case 1 where the heat flux is 442 kW/m², inlet mass rate is 3g/s, inlet temperature is 571.73K and pressure is 5MPa.

In Fig. 8, there is an obvious entrance effect at the inlet of the heating section, that is, the abrupt increase of wall temperature. At $x/d = 10$, wall temperature starts to increase linearly with the increase of the axial distance. As $x/d = 120$, there is a rapid increase of the gradient of wall temperature, indicating that the occurrence of the heat transfer deterioration. From Fig. 8, it can be observed that the heat transfer coefficient decreases as moving downward until a local minimum is reached at $x/d = 60$. Then the heat transfer coefficient begins to slowly recover and reaches to the local maximum at $x/d = 110$, and then the heat transfer coefficient decreases toward the end.

It is noted that the bulk temperature varies nearly linearly with the axial non-dimensional distance. In our previous study [17], the variation of the computed enthalpy of RP-3 with

temperature at 5 MPa was compared with the corresponding experimental data [31], as shown in Fig. 9. It shows that at supercritical pressure the enthalpy increases approximately linearly with the temperature. In order to further demonstrate the critical effect on the enthalpy, Ref. 36 gives the measured enthalpy at different pressures as demonstrated in Fig. 10. As the temperature is beyond the pseudo-critical temperature, the change slope of the enthalpy starts to increase; with pressure increasing, the change of the enthalpy trends to be linear. For constant heat flux case, the bulk enthalpy linearly increases with the non-dimensional distance along the tube due to the energy conservation. The transitivity of the linear relations results in linear variation of the bulk temperature with the axial non-dimensional distance.

In the entire heating section, the fluid bulk temperature is lower than 660 K. The wall temperature corresponding to the local heat transfer coefficient maximum is 660 K and the pseudo-critical temperature at 5 MPa is 716.57 K, implying that it is not only caused by the dramatic change of the thermophysical properties with temperature near the pseudo-critical temperature for heat transfer deterioration.

Fig. 11 shows the fluid temperature, density, axial velocity, viscosity, thermal conductivity and the specific heat varying with the radial distance from the center line of tube at different cross sections, respectively.

In Fig. 11(a), at any cross section, the temperature of the fluids varies dramatically in the neighborhood of the wall and remains basically unchanged in the rest region. Proceeding downstream, the temperature of the fluids rises due to the heating effect by wall heat flux. The intersection of the curves at $x/d = 60$ and $x/d = 120$ leads to the special change of properties.

In Fig. 11(b), at $x/d = 5$, the density in the cross section is rather large, and with moving

downstream, the density gradually decreases. In the certain cross section, the density at the wall is lower than that in the core due to the higher temperature at the wall. Seen from Fig. 11(b), the larger density near the wall occurs at $x/d = 120$ than $x/d = 60$, demonstrating that $x/d = 60$ and $x/d = 120$ correspond to the start points of heat transfer enhancement and heat transfer deterioration, respectively.

It is seen from Fig. 11(c), with moving downstream, the axial velocity increases. This may be caused by the thermal-induced acceleration effect. The velocities near the wall at $x/d = 120$ and $x/d = 160$ are obviously higher than those at $x/d = 5$ and $x/d = 60$, and the large pressure gradient occurs due to the axial thermal acceleration. In order to balance the pressure gradient, the turbulent shear stress in the core region is reduced and the turbulent kinetic energy decreases. Although the flow regime is turbulence, the heat transfer capacity is remarkably suppressed.

It is noted from Figs. 11(d)-(f) that moving downstream, the viscosity decreases, whereas the specific heat increases and the thermal conductivity decreases. Among these three thermophysical properties, the alterations of the viscosity and specific heat promote the enhancement of heat transfer but the change of the thermal conductivity may weaken heat transfer. Actually, due to the thermal-induced acceleration effect, the turbulence is reduced at the certain location and hence the heat transfer deterioration occurs.

In order to further reflect the effect of the variation of the properties on the heat transfer, the variation of the density with temperature along the radial direction for case 1 is shown in Fig. 12. The density computed by the thermophysical property model in Fig. 1 is given in Fig. 12. It gives the obvious representation of the consistency of the thermophysical property model. As proceeding downstream, the density within a cross section alters in a wider density range and a

steeper slope, especially from $x/d = 120$ to $x/d = 160$, replying that thermal-induced acceleration effect leads to the heat transfer deterioration occurring at $x/d = 160$.

Fig. 13 shows the distribution of the Reynolds stress at the flow tangential section for case 1. Moreover, the distribution of the turbulent heat flux at the flow tangential section for case 1 is given in Fig. 14. As the X direction is the mainstream direction, its velocity fluctuation is larger than those in the other two directions, leading to that the Reynolds stresses at UV and UW directions are larger than those at VW directions. The quantitative distribution of UV and UW Reynolds stresses can account for the variation of the heat transfer coefficient along the tube in Fig. 8, that is, large Reynolds stress leads to the large heat transfer coefficient. From Fig. 14, in the mainstream map, the turbulent heat flux increase from the inlet to the outlet along the tube, and at the same flow cross section, the turbulent heat flux near the wall is larger than that in the flow core, indicating that the velocity fluctuation makes more contribution to the distribution of the turbulent heat flux than the temperature fluctuation does.

3.2.2. Case 2: Supercritical temperature case

Fig. 15 shows the variations of the wall temperature, fluid bulk temperature and corresponding heat transfer coefficient with the non-dimensional distance by LES for case 2. It is seen that the slight entrance effects exist in wall temperature with the following linear growth. The heat transfer coefficient decreases with the increasing non-dimensional distance. Case 2 can be regarded as the supercritical temperature case due to the high fluid bulk temperature, which almost exceeds the pseudo-critical temperature at 5 MPa. At $x/d = 25$, the wall temperature reaches the pseudo-critical temperature, meanwhile, the fluid temperature near wall comes close to the pseudo-critical temperature, where the thermophysical properties change significantly leading to

the occurrence of heat transfer deterioration after $x / d = 25$.

Fig. 16 shows the fluid temperature varying with the radial distance from the center line of the tube at different cross sections. As moving downstream, the fluid temperature increases. The typical turbulent heat exchange situation exists in terms of the temperature profile, meaning that no remarkable heat transfer deterioration occurs in the main part of tube (seen in Fig. 15).

3.2.3. Case 3: Subcritical temperature case

Fig. 17 gives the variations of the wall temperature, fluid bulk temperature and corresponding heat transfer coefficient with the non-dimensional distance by LES for case 3. As seen from Fig. 17, similar to that of case 1, the obvious entrance effect occurs until $x / d = 30$ and the wall temperature increases monotonically, without the rise of the wall temperature at the second half of the tube. Compared with case 1, the scope of the obvious entrance effect in the inlet heating section in case 3 has the united ending temperature of about 625 K.

With the non-dimensional distance increasing, the heat transfer coefficient at the cross section abruptly decreases at the inlet, then reaches to the local minimum at $x / d = 40$ followed by the slow upturn. Beyond $x / d = 60$, the convective heat transfer coefficient keeps almost unchanged. Due to that in the entire tube both wall temperature and bulk temperature are lower than pseudo-critical temperature, the drastic change of the thermophysical properties in the vicinity of pseudo-critical temperature may be not the reason for the heat transfer phenomenon in case 3.

The radial variations of the fluid temperature, density, viscosity, thermal conductivity and specific heat at different axial locations for case 3 are given in Fig. 18. In Fig. 18(a), as proceeding downstream, the temperature of the fluids near the wall rises due to the wall heating. The

intersection of the curves at $x/d = 40$ and $x/d = 60$ leads to the special change of the properties as follows. As moving downstream, the density gradually decreases, also the same rule exists near the wall. However, the unexpected phenomena appears at $x/d = 60$ where the density near the wall is larger than that at $x/d = 40$, resulting in the local heat transfer deterioration and recovery in Fig. 17. Ranging from the heating section inlet to the location of the heat transfer coefficient minimum, the density, viscosity and thermal conductivity near the wall decrease, but the specific heat increases. Among these four factors, only the change of the thermal conductivity makes contribution to the heat transfer weakened with the rest factors making heat transfer enhanced, meaning that the thermal conductivity plays a significant role in leading to the heat transfer deterioration in the entrance effect. In the inlet of heating section, the thermal boundary layer is developing and its thickness is accumulated. Due to the thermal conductivity decreases with the increasing temperature, the large thermal resistance is formed to make the small change of the fluid temperature, hence small change of the fluid velocity. The heat exchange between the fluid core and wall is suppressed leading to the abrupt increase of wall temperature at the inlet of heating section.

In order to distinctly exhibit the critical effect on the heat transfer, the comparison of the heat transfer characteristics in three cases is given in Fig. 19. It is seen that to keep away from the pseudo-critical point can reduce the occurrence of the heat transfer deterioration. While for the lower inlet temperature case, the wall temperature can reach to the larger value due to the heat transfer deterioration. In case 2, if ignoring the heat transfer deterioration at the tail of tube, it can get the largest heat transfer coefficient among three cases.

In the future work, the worse heat transfer deterioration case should be investigated

numerically to grasp the detailed mechanisms; meanwhile, a more precise and faster RANS method will be put forward for the engineering application of supercritical heat transfer. The corresponding experiment should be carried out to obtain the empirical correlation of onset of the heat transfer deterioration, in order to assisting the design of regenerative cooling system.

4. Conclusions

In the present study, a LES method is employed to study the convective heat transfer of aviation kerosene RP-3 flowing in the miniature round tube under three different cases, and comparing LES results with available experimental data as well as other turbulence model results.

Major findings of this study are as follows:

- (1) Compared with RANS, LES gives the better performance in predicting the wall temperature and the total pressure drop against the experimental results. The pressure drop obtained by LES is larger than that by RANS, and it is opposite for the wall temperature.
- (2) For the subcritical, transcritical and supercritical temperature cases, the entrance effect occurs at the inlet of the heating section, that is, the abruptly increasing wall temperature and the reduced heat transfer coefficient. On account of the developing thermal boundary layer and relatively slow flow velocity, heat transfer deterioration occurs in which the change of the thermal conductivity plays an important role.
- (3) The significant alteration of the thermophysical properties in the vicinity of the pseudo-critical temperature at supercritical pressure leads to the severe thermal-induced acceleration effect of RP-3 at the transcritical case. The large pressure gradient is created and turbulence intensity weakens resulting in the impaired heat exchange between the

wall and the flow core. Compared with the temperature fluctuation, the velocity fluctuation has a greater impact on the supercritical heat transfer.

Acknowledgement

The authors gratefully acknowledge funding support from Program for National Natural Science Foundation of China (No. 51406005).

References

- [1] Berche B, Henkel M, Kenna R. Critical phenomena: 150 years since Cagniard de la Tour. *Revista Brasileira De Ensino De Física*, 2009, 13(3):2602.1-2602.4.
- [2] Reiss T, Csom G, Fehér S, et al. The simplified supercritical water-cooled reactor (SSCWR), a new SCWR design. *Progress in Nuclear Energy*, 2010, 52(2): 177-189.
- [3] Jusko W J, Levy G. Effect of buoyancy and flow acceleration on heat transfer of supercritical CO₂ in natural circulation loop[J]. *International Journal of Heat & Mass Transfer*, 2015, 91(9):640-646.
- [4] Qin J, Zhang S, Bao W, et al. Thermal management method of fuel in advanced aeroengines. *Energy*, 2013, 49: 459-468.
- [5] Edwards T. USAF supercritical hydrocarbon fuels interests. AIAA paper, 1993, 93.
- [6] Curran E T. Scramjet engines: the first forty years. *Journal of Propulsion and Power*, 2001, 17(6): 1138-1148.
- [7] Jackson J D. Fluid flow and convective heat transfer to fluids at supercritical pressure. *Nuclear Engineering and Design*, 2013, 264: 24-40.
- [8] Lei X, Li H, Dinh N, et al. A study of heat transfer scaling of supercritical pressure water in horizontal tubes[J]. *International Journal of Heat & Mass Transfer*, 2017, 114:923-933.
- [9] Yamagata K, Nishikawa K, Hasegawa S, et al. Forced convective heat transfer to supercritical water flowing in tubes. *International Journal of Heat and Mass Transfer*, 1972, 15(12):2575-2593.
- [10] Zhang C, Xu G, Gao L, et al. Experimental investigation on heat transfer of a specific fuel (RP-3) flows through downward tubes at supercritical pressure. *Journal of Supercritical*

Fluids, 2012, 72(9):90-99.

- [11] Schiestel, Roland. Modeling and simulation of turbulent flows. Wiley, 2008.
- [12] Zhu J, Tao Z, Deng H, et al. Numerical investigation of heat transfer characteristics and flow resistance of kerosene RP-3 under supercritical pressure. International Journal of Heat and Mass Transfer, 2015, 91:330-341.
- [13] He S, Kim W S, Jiang P X, et al. Simulation of mixed convection heat transfer to carbon dioxide at supercritical pressure. ARCHIVE Proceedings of the Institution of Mechanical Engineers Part C Journal of Mechanical Engineering Science 1989-1996 (vols 203-210), 2004, 218(11):1281-1296.
- [14] Tang G, Shi H, Wu Y, et al. A variable turbulent Prandtl number model for simulating supercritical pressure CO₂ heat transfer[J]. International Journal of Heat & Mass Transfer, 2016, 102:1082-1092.
- [15] Pandey S, Xu C, Laurien E. Investigation of in-tube cooling of carbon dioxide at supercritical pressure by means of direct numerical simulation[J]. International Journal of Heat & Mass Transfer, 2017, 114:944-957.
- [16] Bae J H, Yoo J Y, Choi H. Direct numerical simulation of turbulent supercritical flows with heat transfer. Physics of Fluids, 2005, 17(10):465-380.
- [17] Bae J H, Yoo J Y, McEligot D M. Direct numerical simulation of heated CO₂ flows at supercritical pressure in a vertical annulus at Re=8900[J]. Physics of Fluids, 2008, 20(5):34-43.
- [18] He S, Kim W S, Bae J H. Assessment of performance of turbulence models in predicting supercritical pressure heat transfer in a vertical tube. International Journal of Heat and Mass Transfer, 2008, 51(19–20):4659-4675.
- [19] Srivastava S, Jaber F. Large eddy simulations of complex multicomponent diesel fuels in high temperature and pressure turbulent flows[J]. International Journal of Heat & Mass Transfer, 2017, 104:819-834.
- [20] Wang X, Xu X, Pletcher R. Large eddy simulation of supercritical CO₂ pipe flow with constant wall heat flux. Aiaa Computational Fluid Dynamics Conference. 2005:739–749.

- [21] B. Ničeno, M. Sharabi. Large eddy simulation of turbulent heat transfer at supercritical pressures. *Nuclear Engineering and Design*, 2013, 261(8):44-55.
- [22] Azimov U B, Kim K S. Large-eddy simulation of air entrainment during diesel spray combustion with multi-dimensional CFD. *International Journal of Automotive Technology*, 2011, 12(6):795-812.
- [23] Dagaut P, Cathonnet M. The ignition, oxidation, and combustion of kerosene: A review of experimental and kinetic modeling. *Progress in Energy and Combustion Science*, 2006, 32(1):48-92.
- [24] Huber, M. L. NIST Thermophysical Properties of Hydrocarbon Mixtures Database (SUPERTRAPP). Us Department of Commerce. 2012.
- [25] Tao Z, Cheng Z, Zhu J, et al. Effect of turbulence models on predicting convective heat transfer to hydrocarbon fuel at supercritical pressure. *Chinese Journal of Aeronautics*, 2016, 29(5):1247-1261.
- [26] Zhang C B. Investigation of flow and heat transfer characteristics of hydrocarbon fuel at supercritical pressures, PhD thesis, Beijing University of Aeronautics and Astronautics, Beijing, China, 2011.
- [27] Wagner C D, Hüttl T, Sagaut P. Large-eddy simulation for acoustics[M]. Cambridge University Press, 2007.
- [28] Lilly DK. The representation of small-scale turbulence in numerical simulation experiments. In: *Proceedings of IBM scientific computing symposium on environmental science*, NY; 1967: 195–210.
- [29] I. Fluent ANSYS FLUENT 14.5.0: User's Guide Fluent Inc., Lebanon, N.H. 2012.
- [30] Kondo K, Murakami S, Mochida A. Generation of Velocity Fluctuations for Inflow Boundary Condition of LES. *Journal of Wind Engineering and Industrial Aerodynamics*, 1997, 67: 51-64
- [31] Zhang C B, Deng H W, Guo-Qiang X U, et al. Enthalpy measurement and heat transfer investigation of RP-3 kerosene at supercritical pressure[J]. *Journal of Aerospace Power*, 2010, 25(2):331-335.

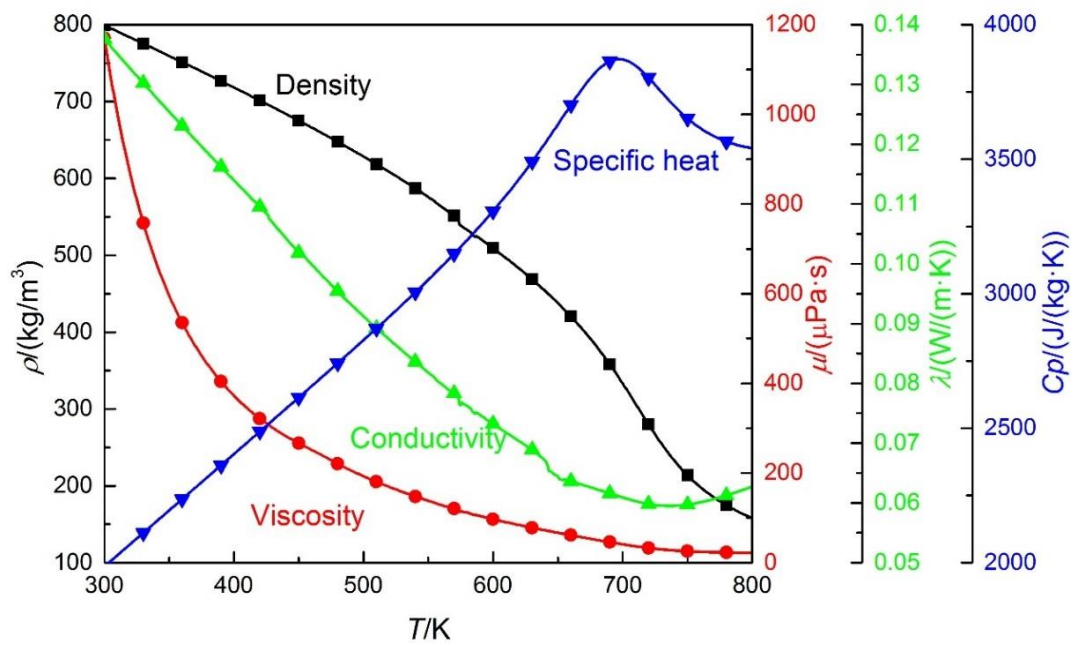
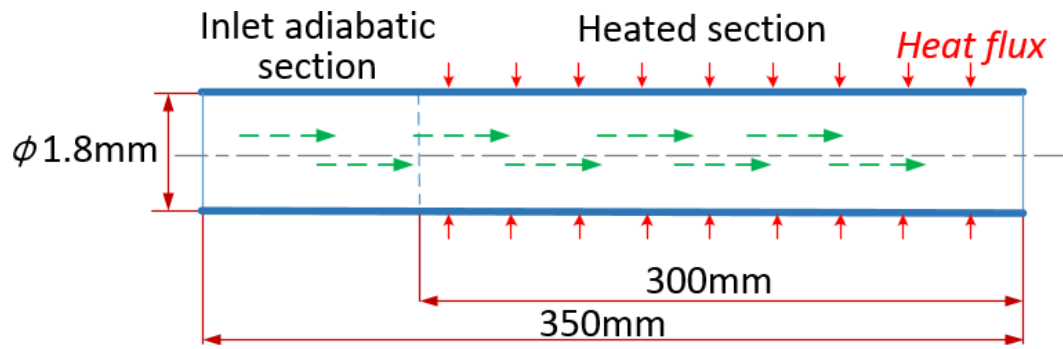
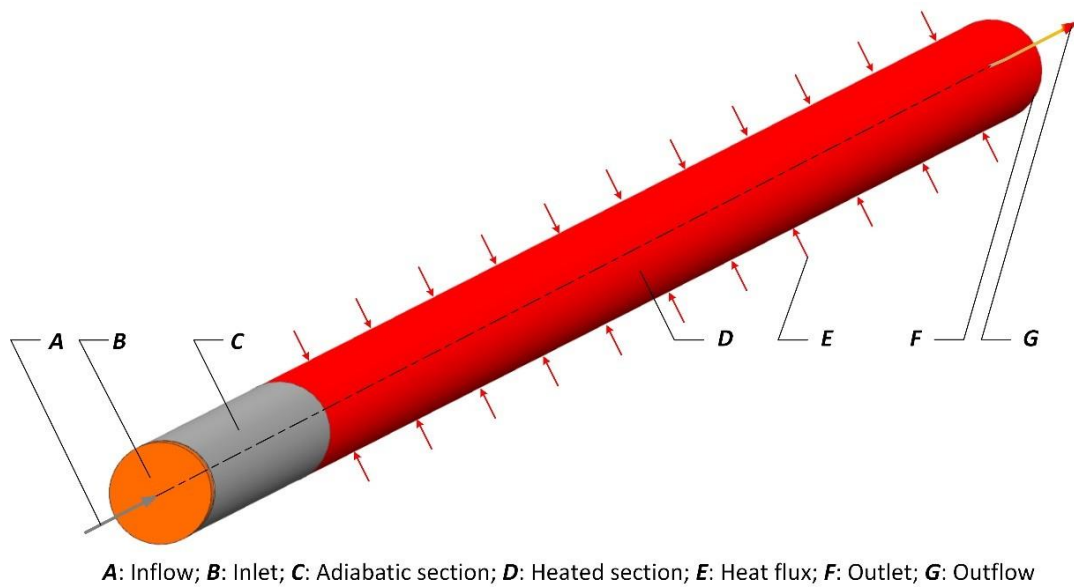


Fig. 1. Thermophysical properties of four-species surrogate model of RP-3 varying with temperature at 5MPa.



(a) Schematic of the flow tangential section of the computational domain.



(b) Physical model.

Fig. 2. Schematic diagram of the computational model.

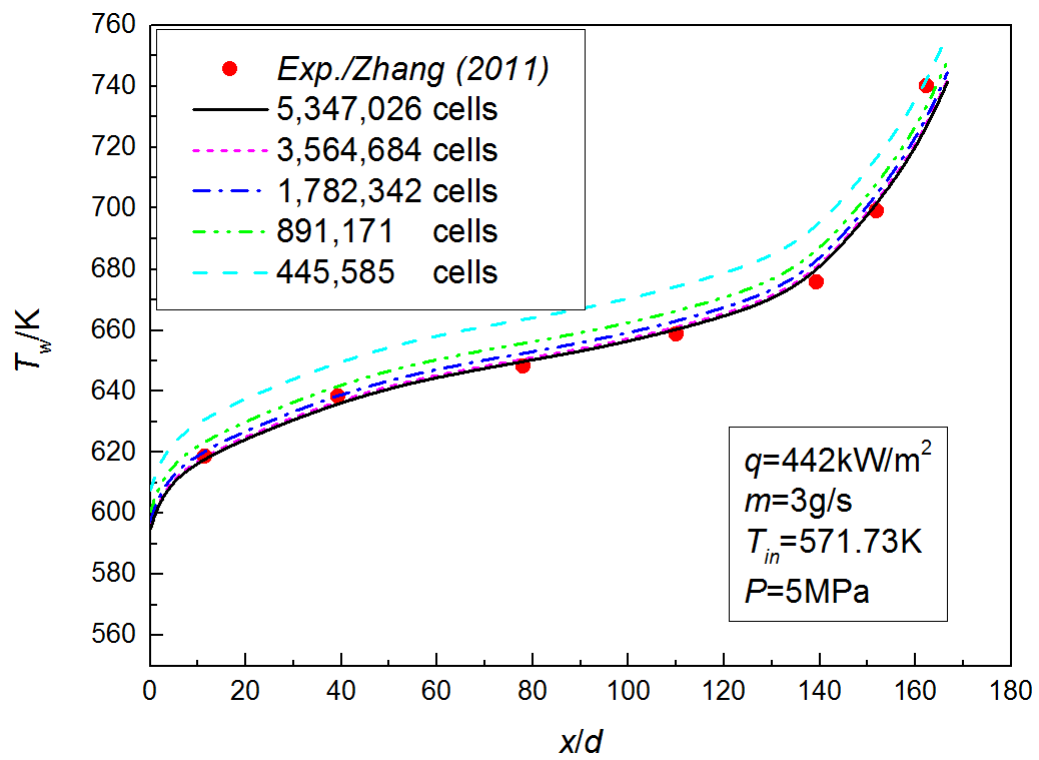
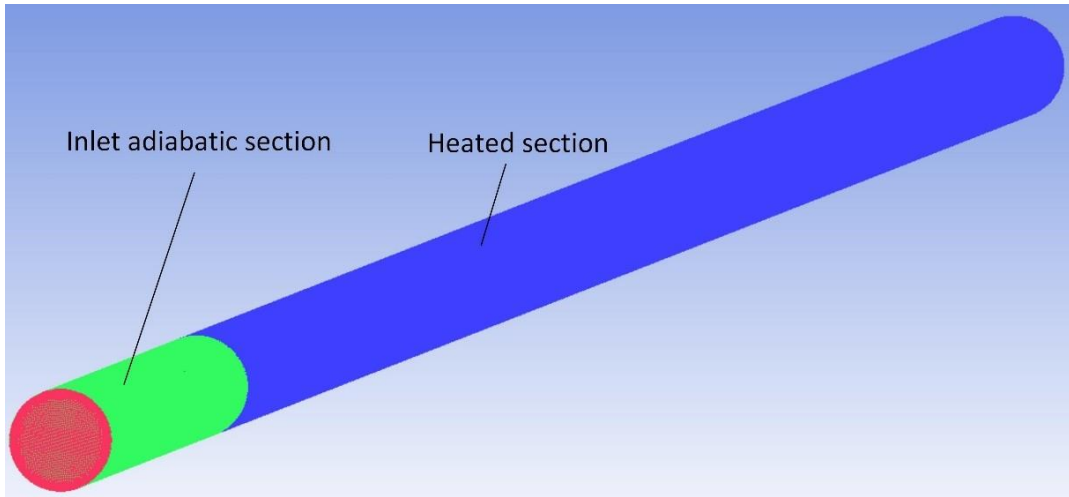
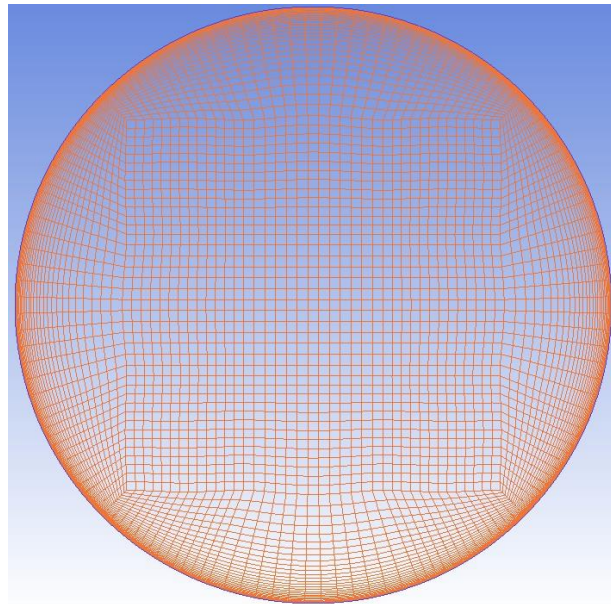


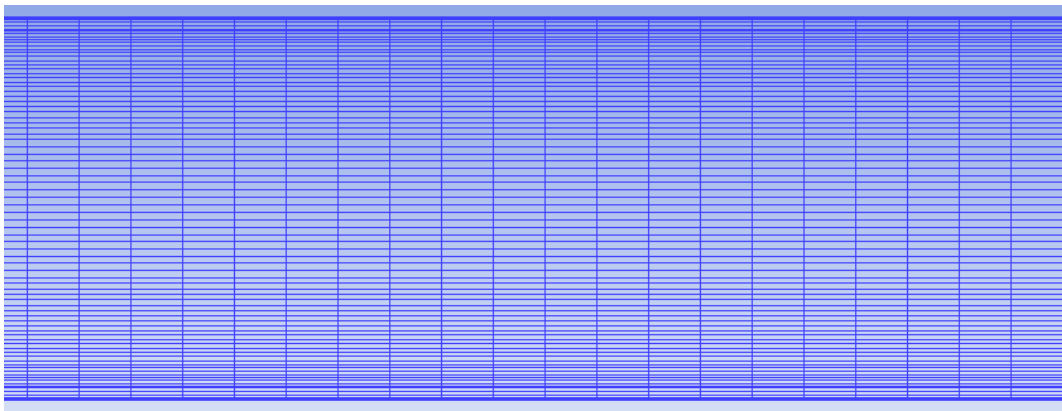
Fig. 3. Grid independence for LES.



(a) Schematic of the mesh of the computational domain.

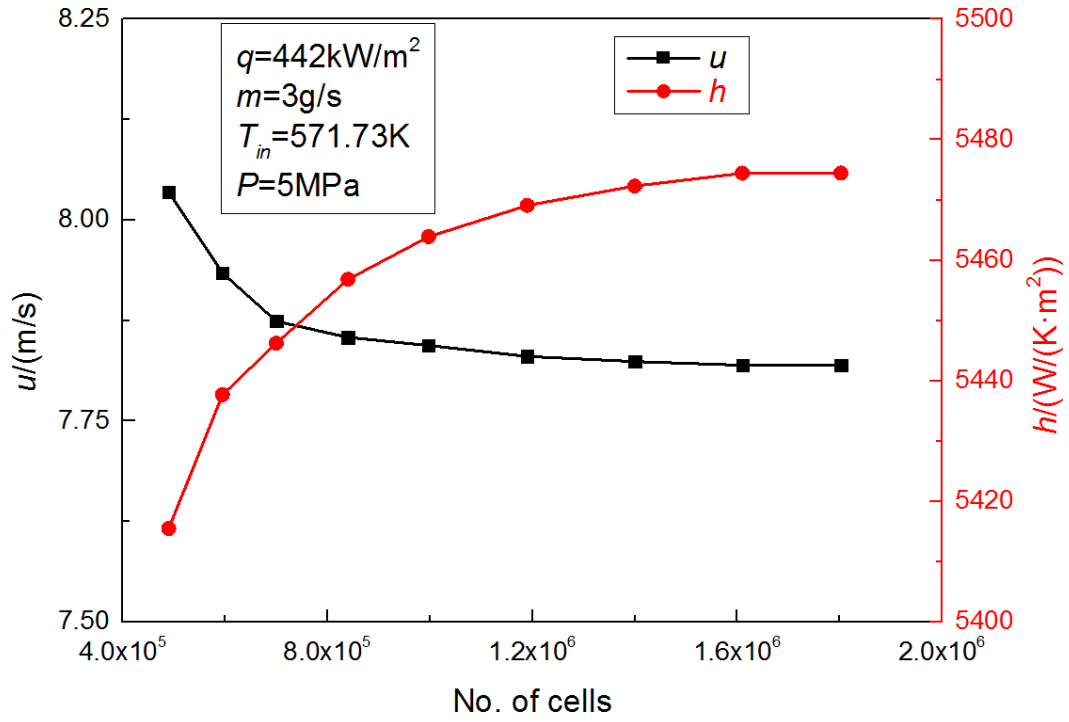


(b) View of cross section mesh.

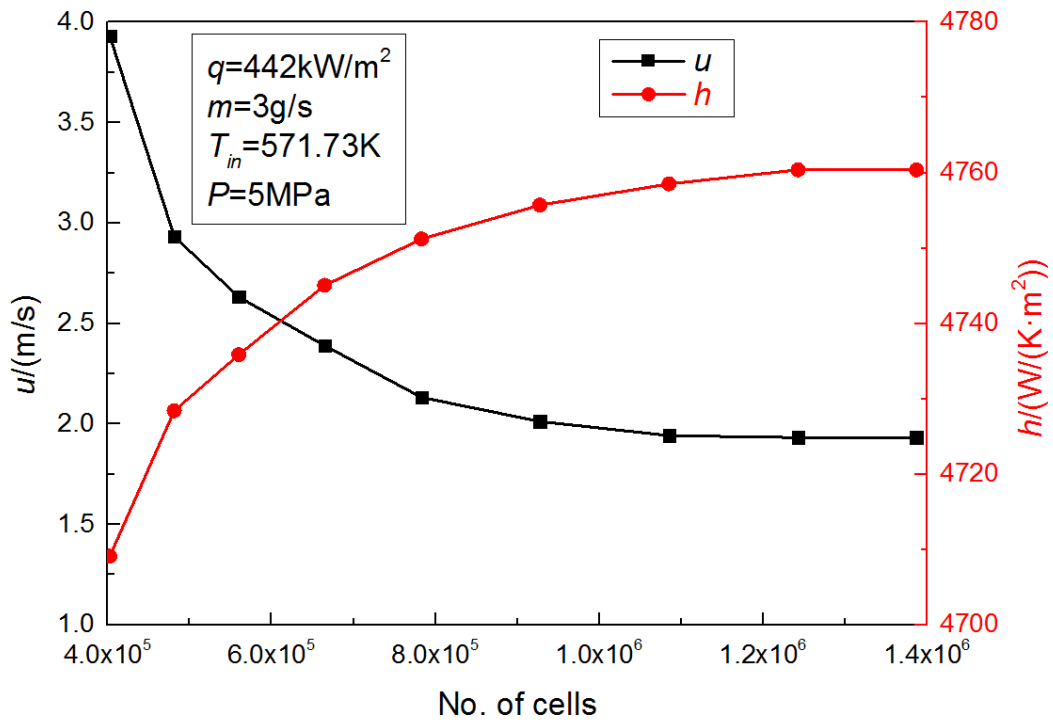


(c) Local view of the flow tangential section mesh.

Fig. 4. Mesh of the computational model.

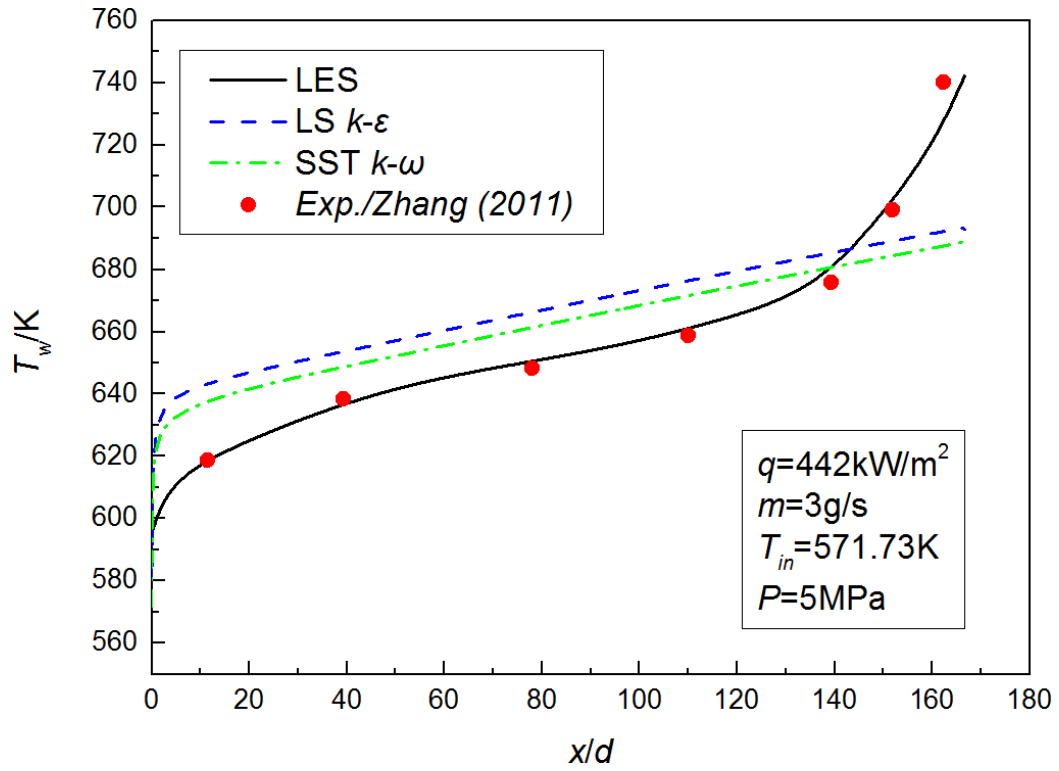


(a) LS $k-\epsilon$

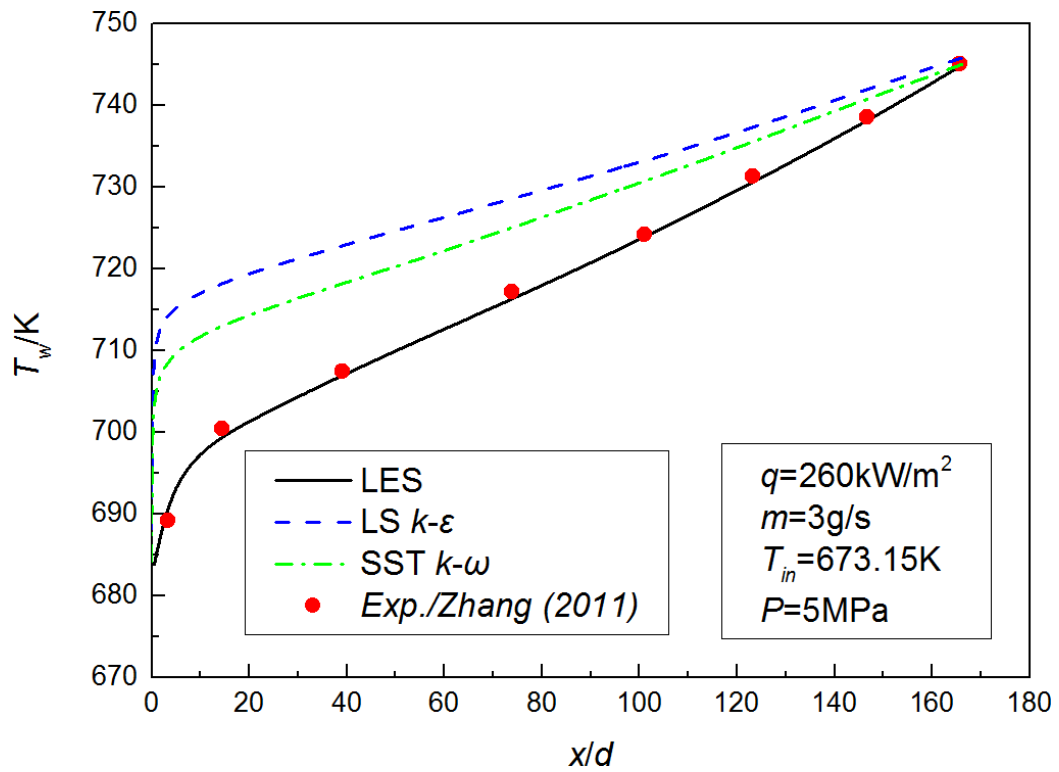


(b) SST $k-\omega$

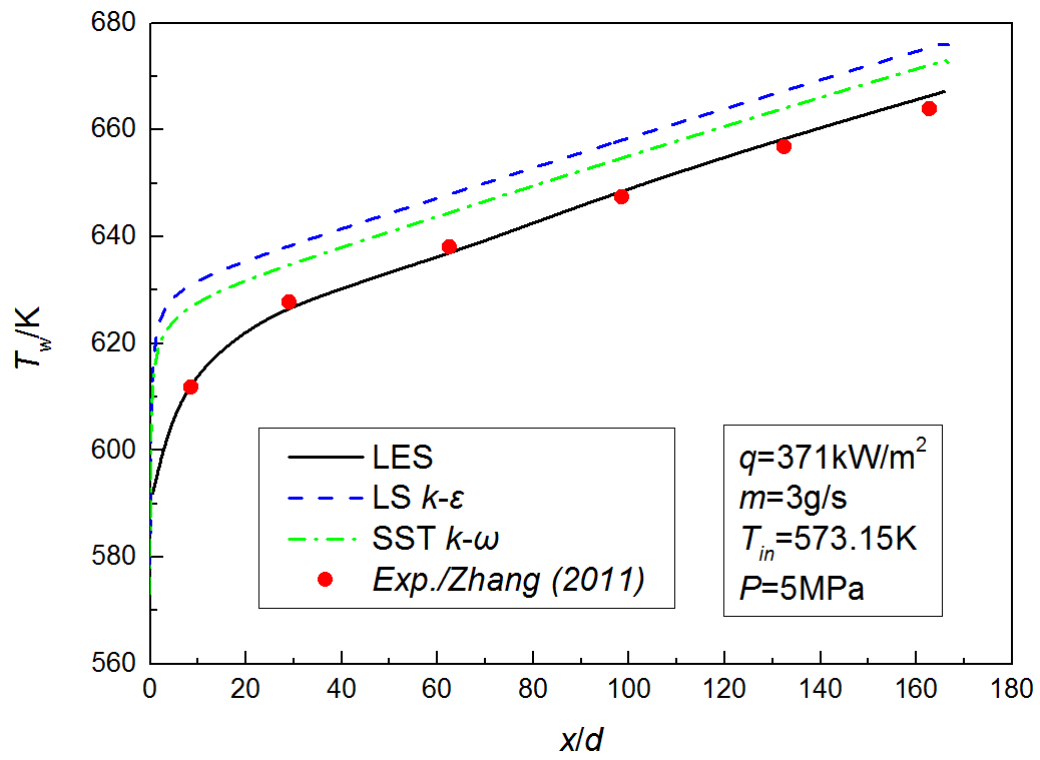
Fig. 5. Grid independence for RANS models.



(a) Case 1

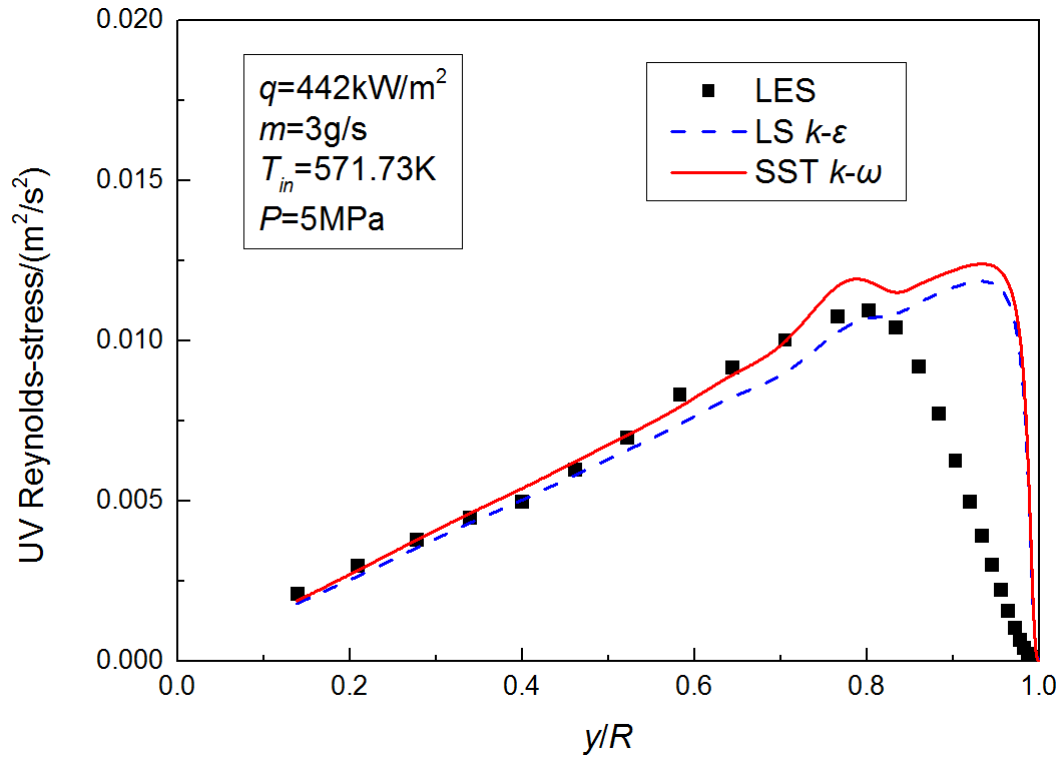


(b) Case 2

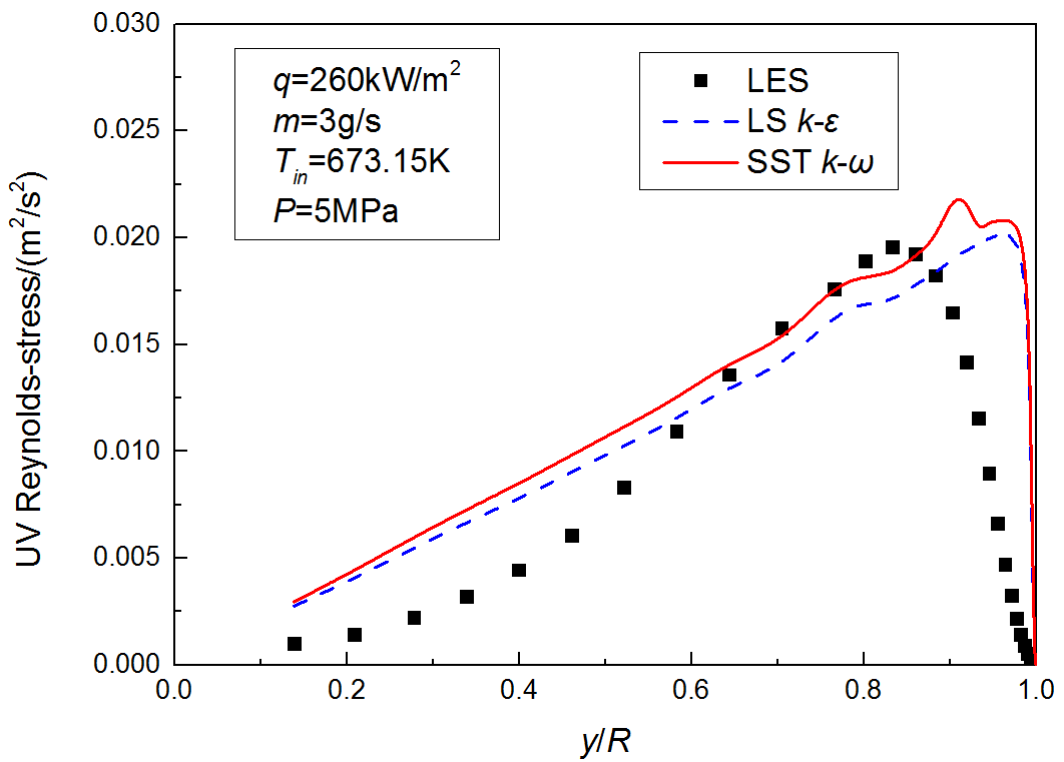


(c) Case 3

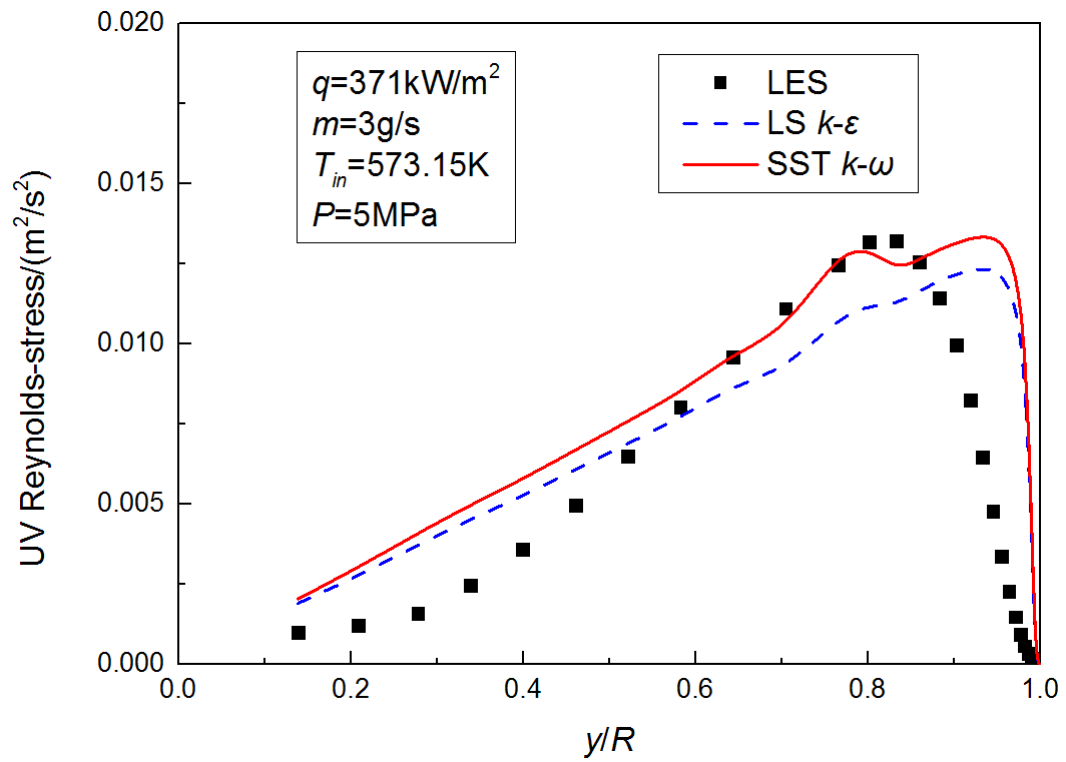
Fig. 6. Comparison between the calculated wall temperatures and the experimental results (both LES and RANS are included).



(a) Case 1



(b) Case 2



(c) Case 3

Fig. 7. Comparison of the calculated UV Reynolds-stress by different models.

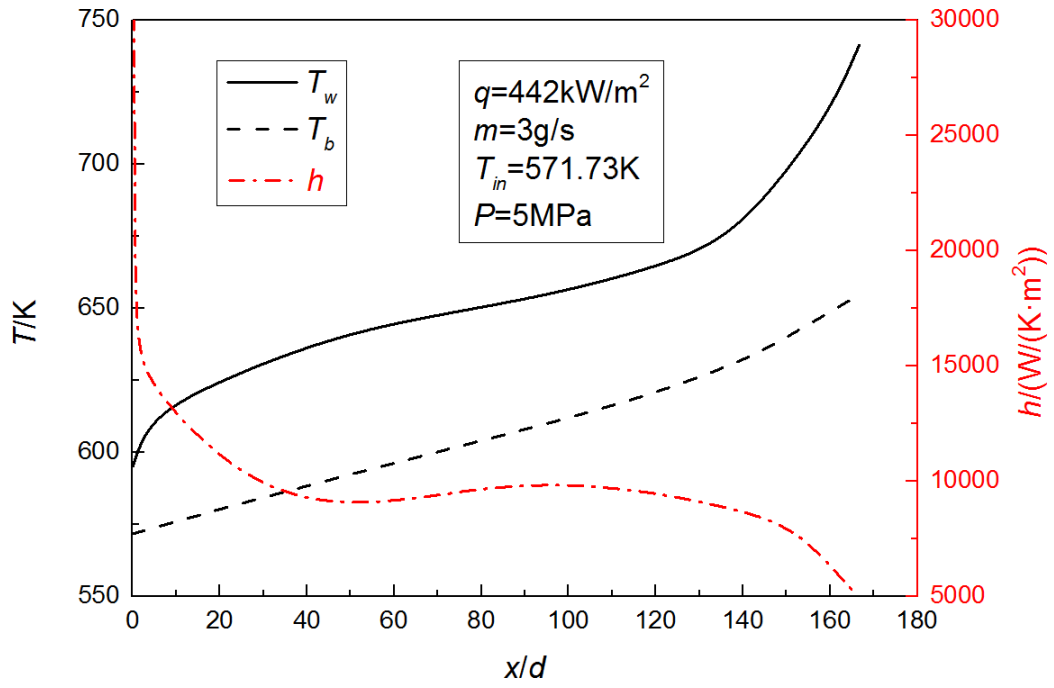


Fig. 8. Variations of the wall temperature, fluid bulk temperature and corresponding heat transfer coefficient with the non-dimensional distance by LES for case 1.

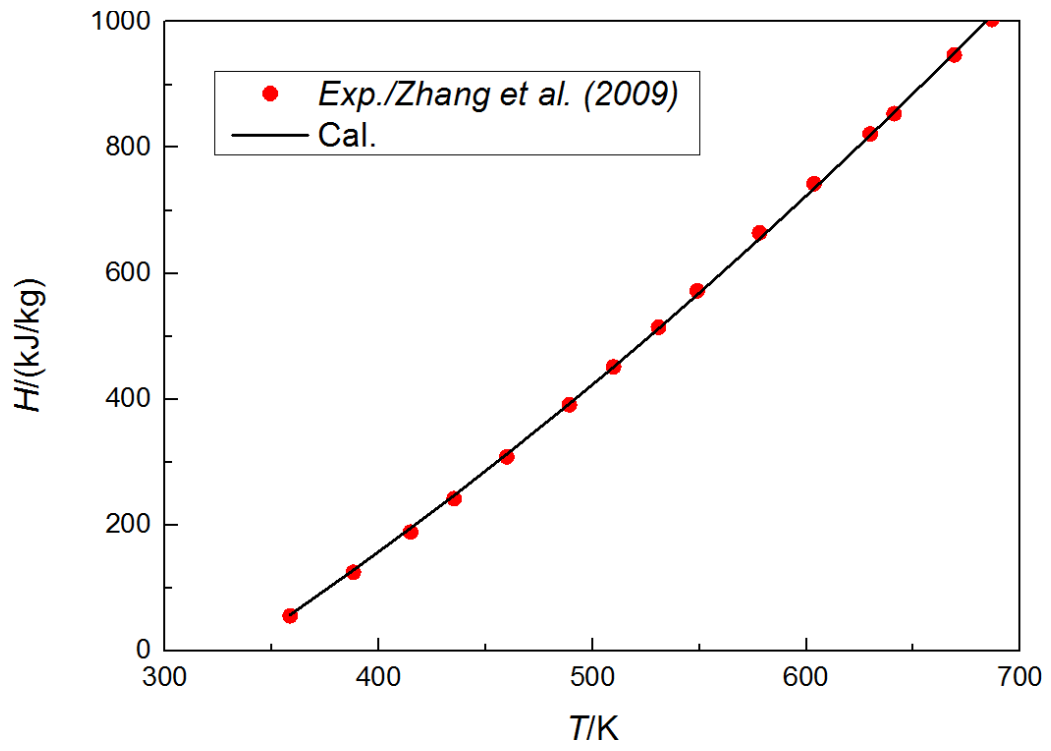


Fig. 9. Variation of computed enthalpy of RP-3 with temperature at 5MPa [17].

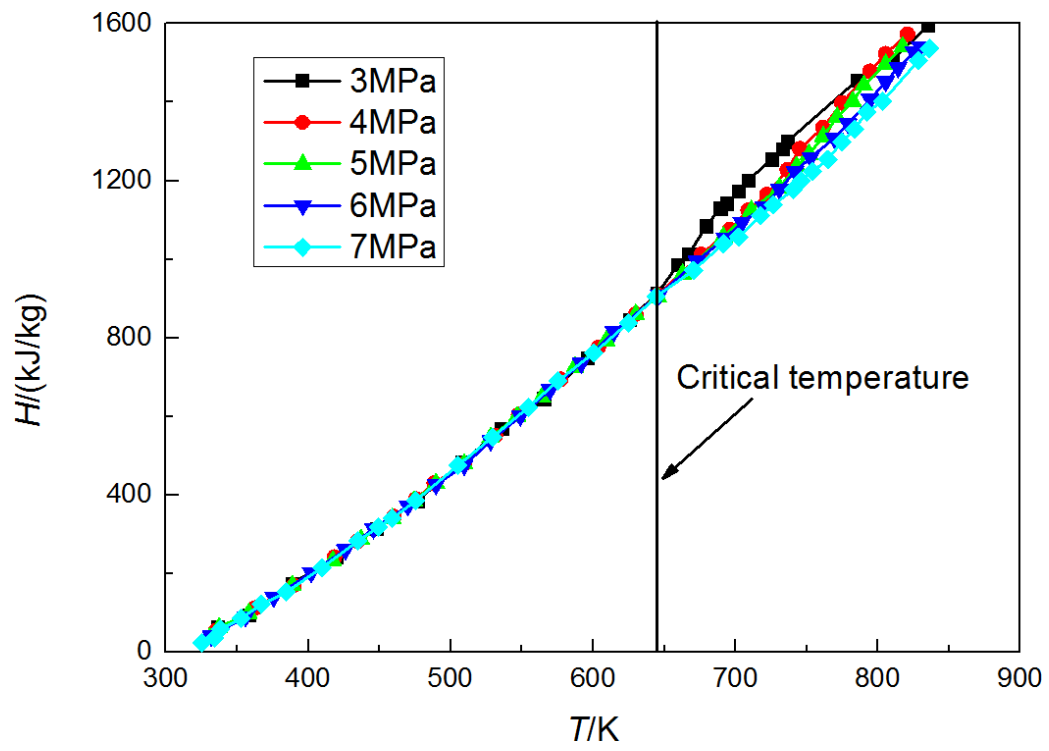
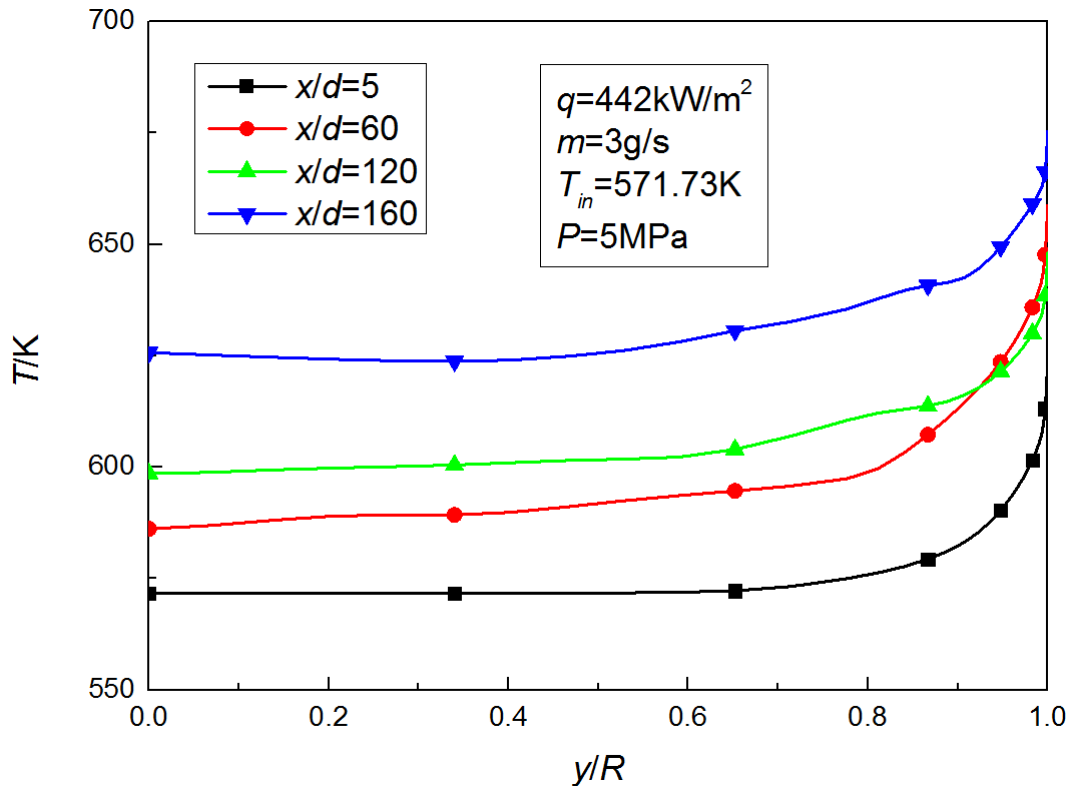
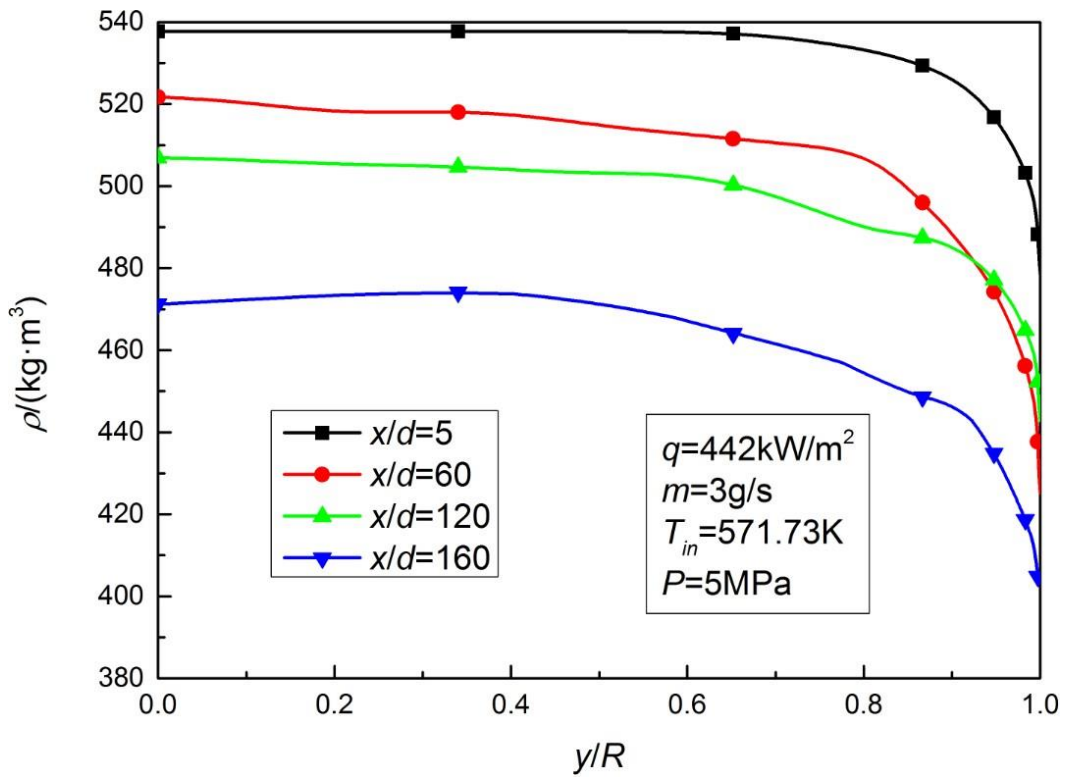


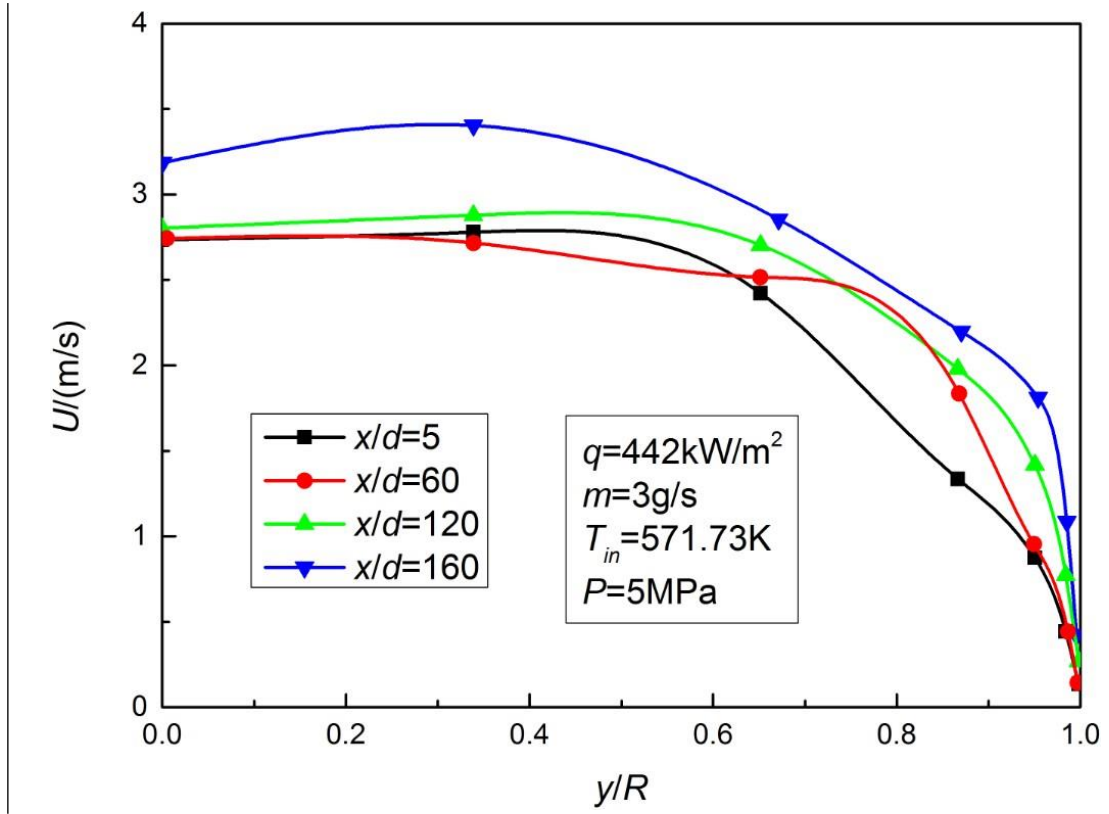
Fig. 10. Variation of measured enthalpy of RP-3 with temperature at different pressures [36].



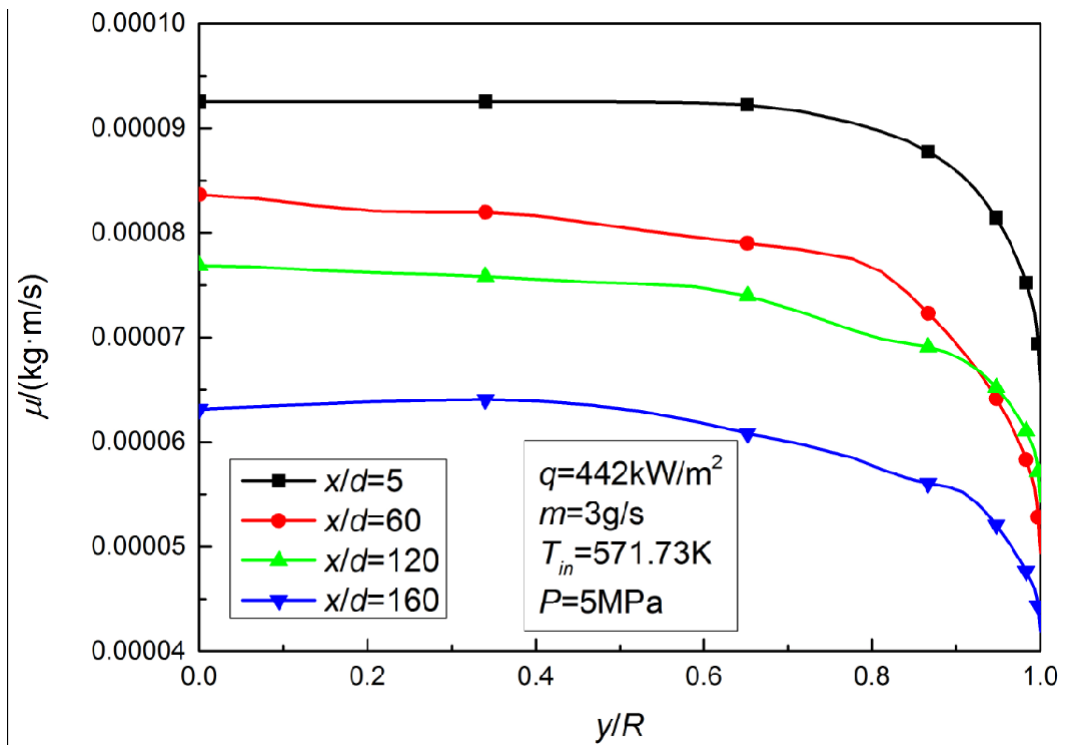
(a) Fluid temperature



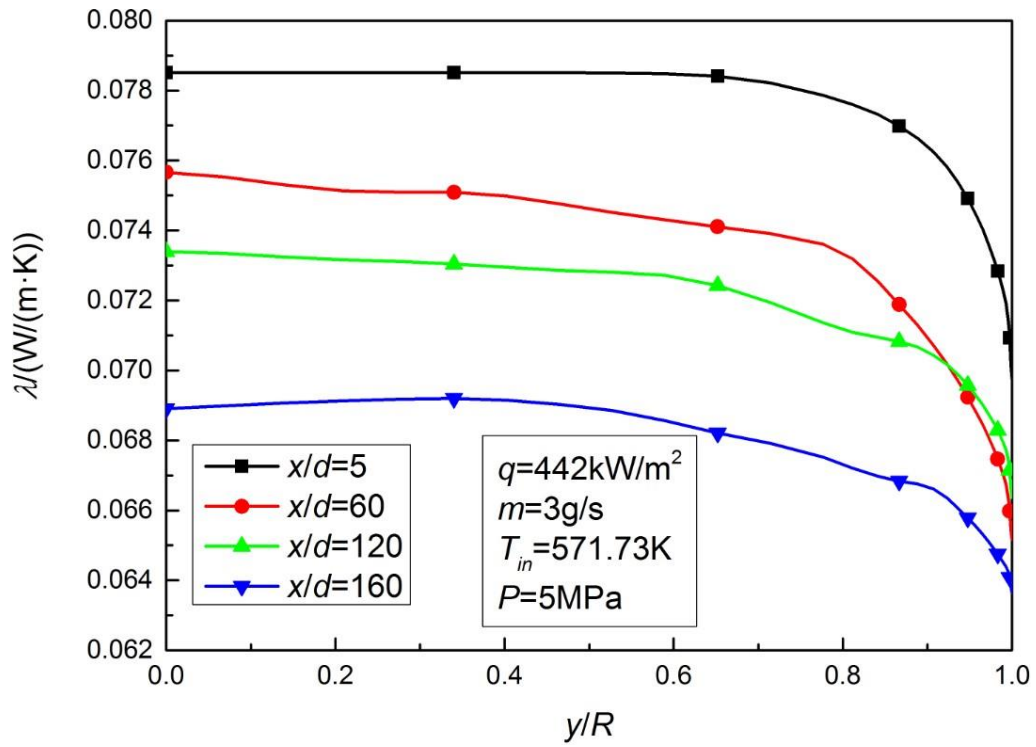
(b) Density



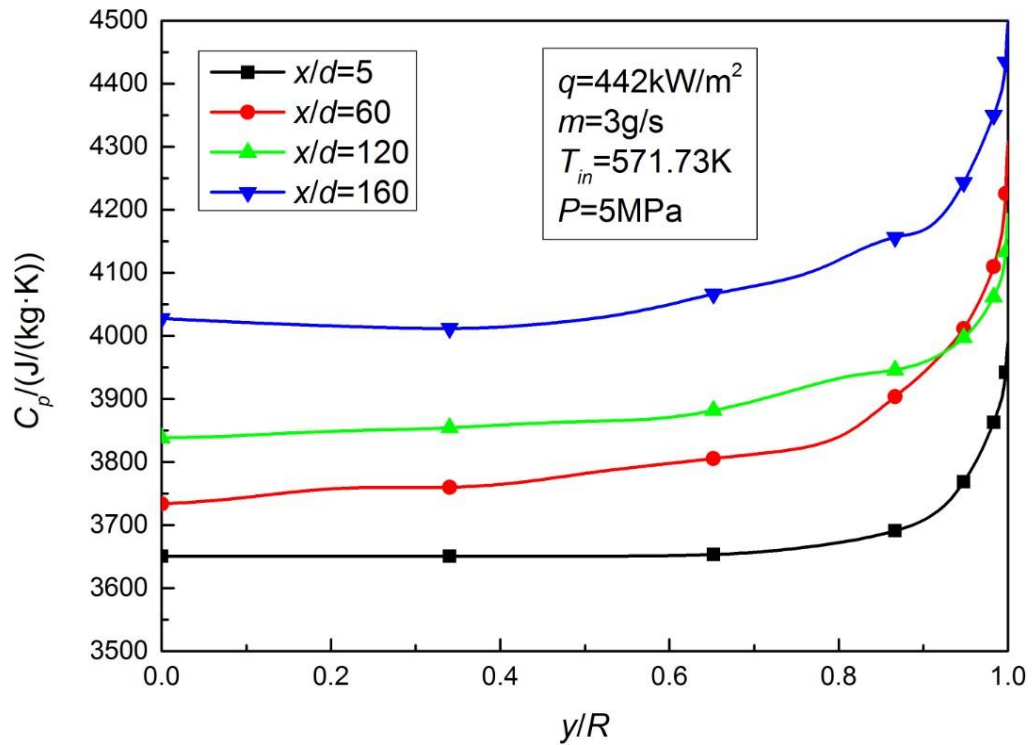
(c) Axial velocity



(d) Viscosity



(e) Thermal conductivity



(f) Specific heat

Fig. 11. Radial variation of six different physical parameters at different axial locations along the pipe for case 1.

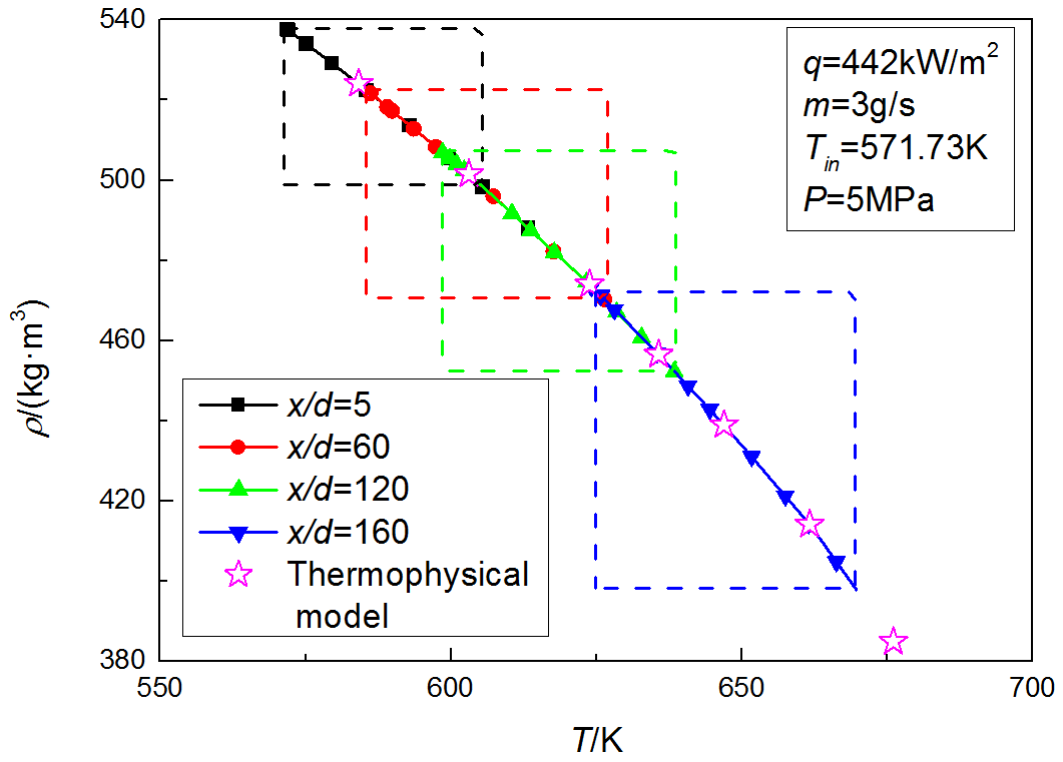


Fig. 12. Variation of density with temperature along the radial direction for case 1.

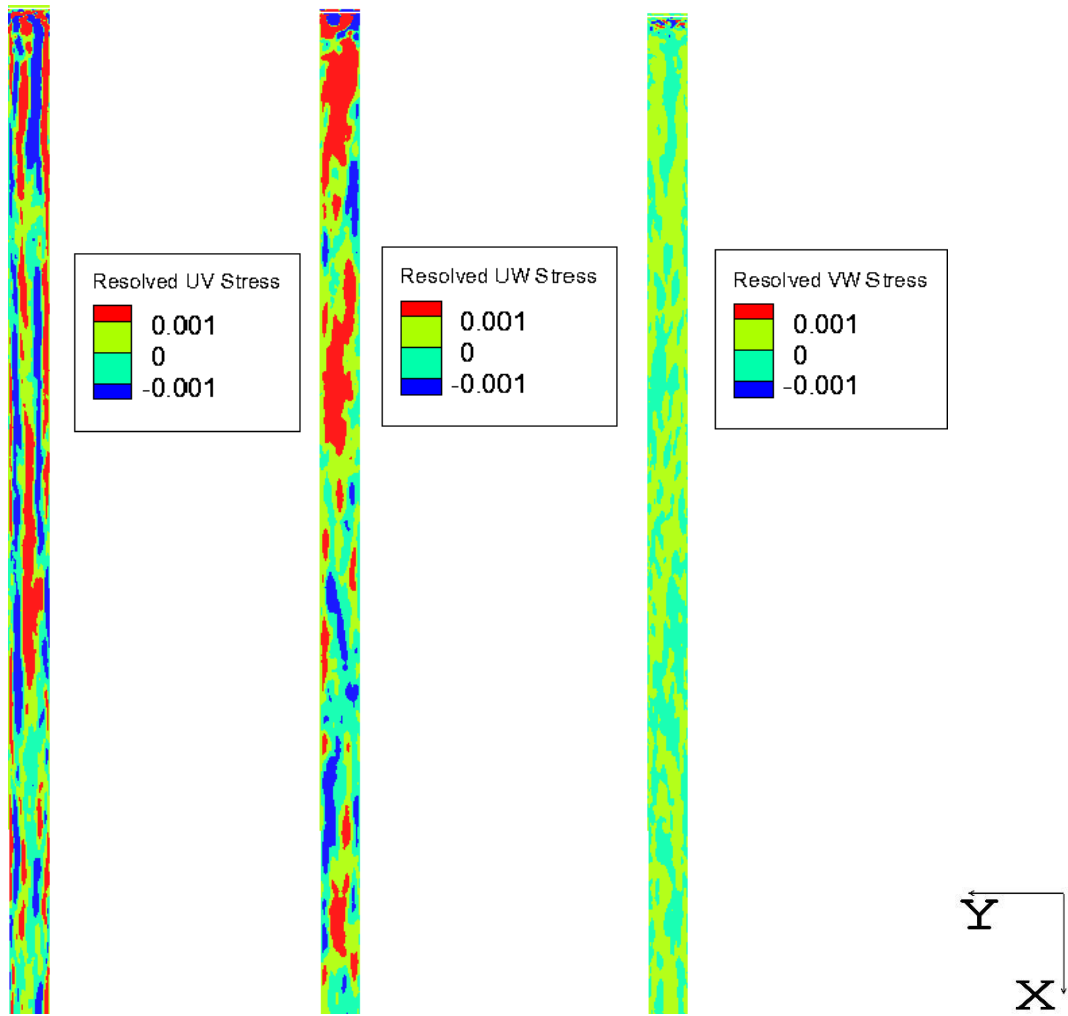


Fig. 13. Distribution of Reynolds stress (unit: m^2/s^2) at the flow tangential section for case 1.

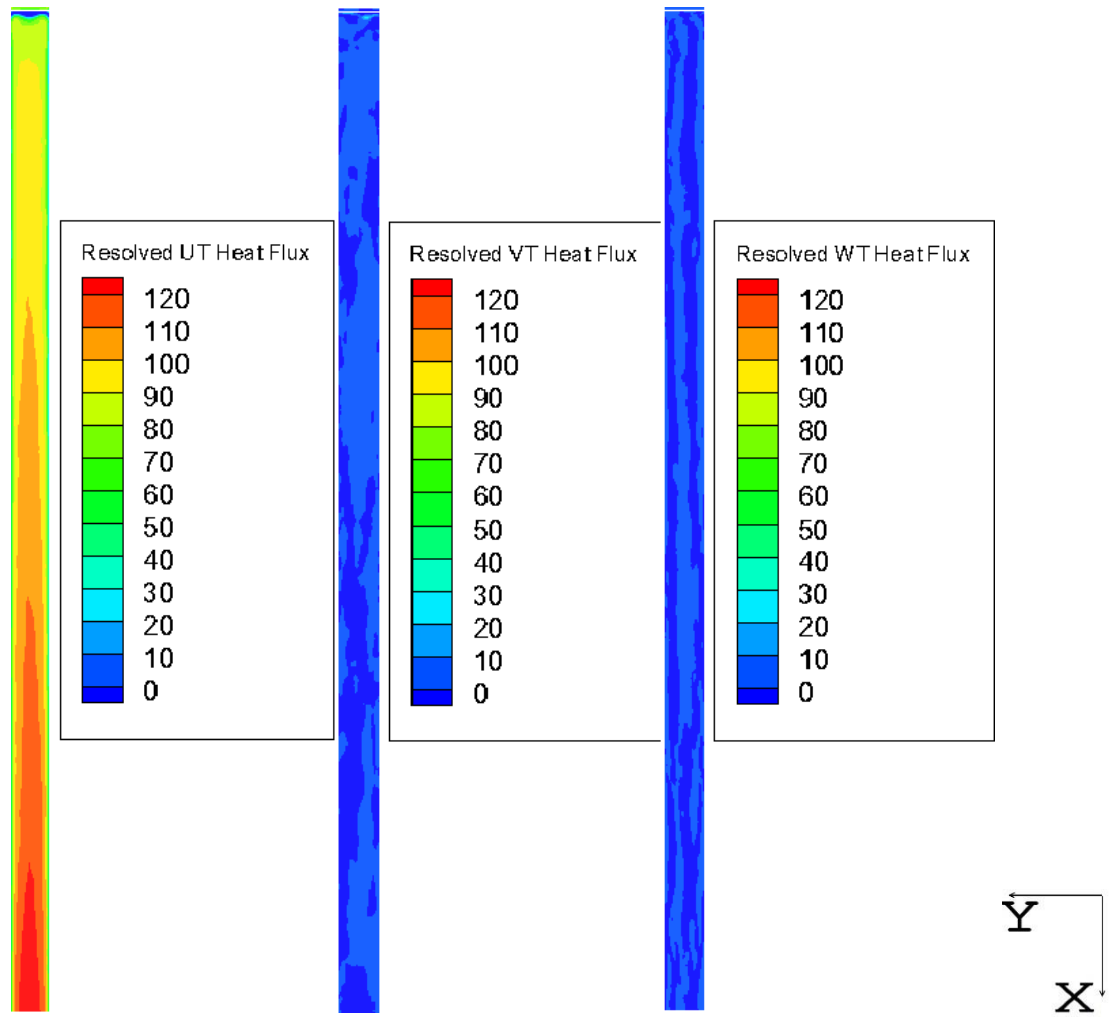


Fig. 14. Distribution of turbulent heat flux (unit: $\text{m}\cdot\text{k}/\text{s}$) at the flow tangential section fro case 1.

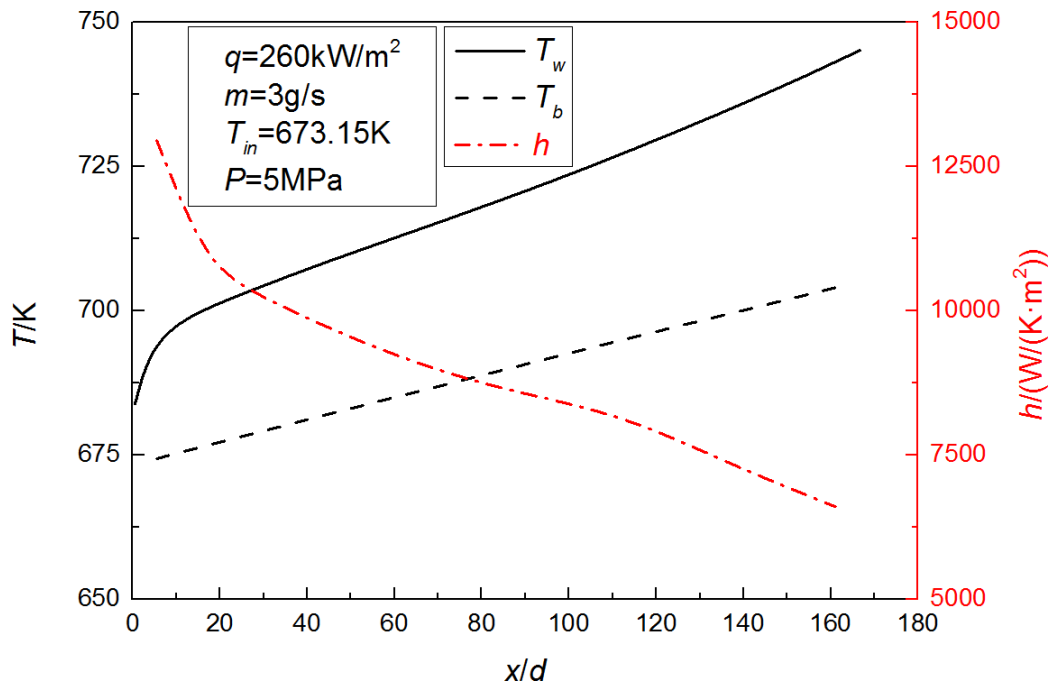


Fig. 15. Variations of the wall temperature, fluid bulk temperature and corresponding heat transfer coefficient with the non-dimensional distance by LES for case 2.

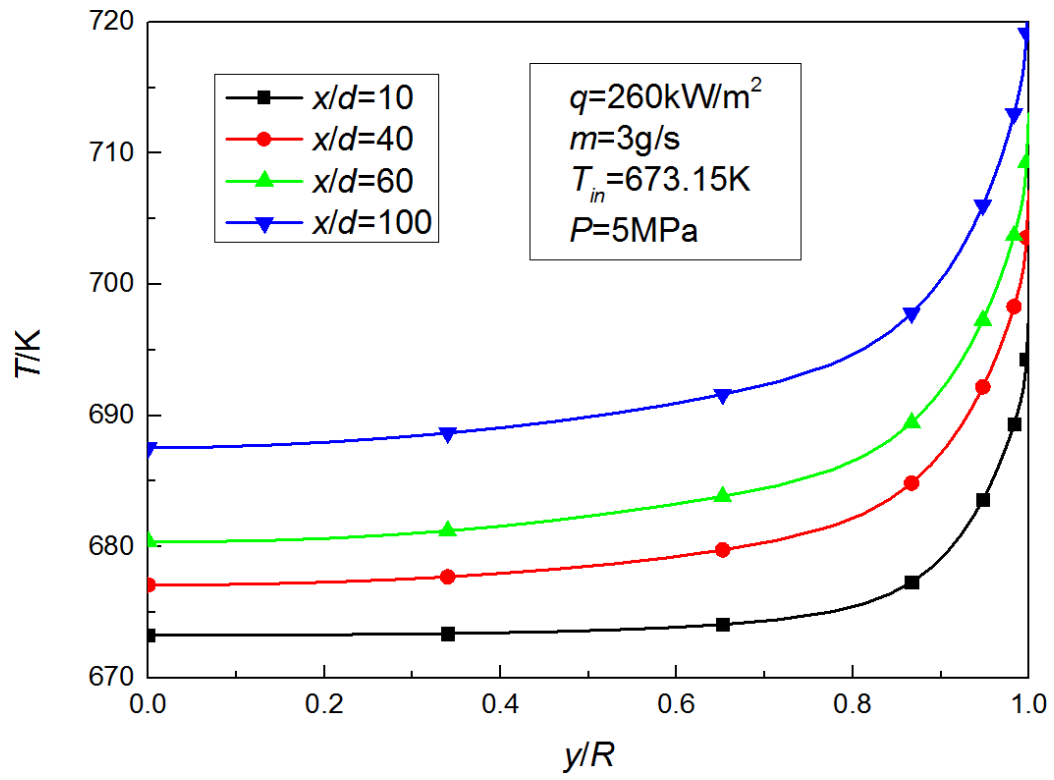


Fig. 16. Radial variation of the fluid temperature at different axial locations for case 2.

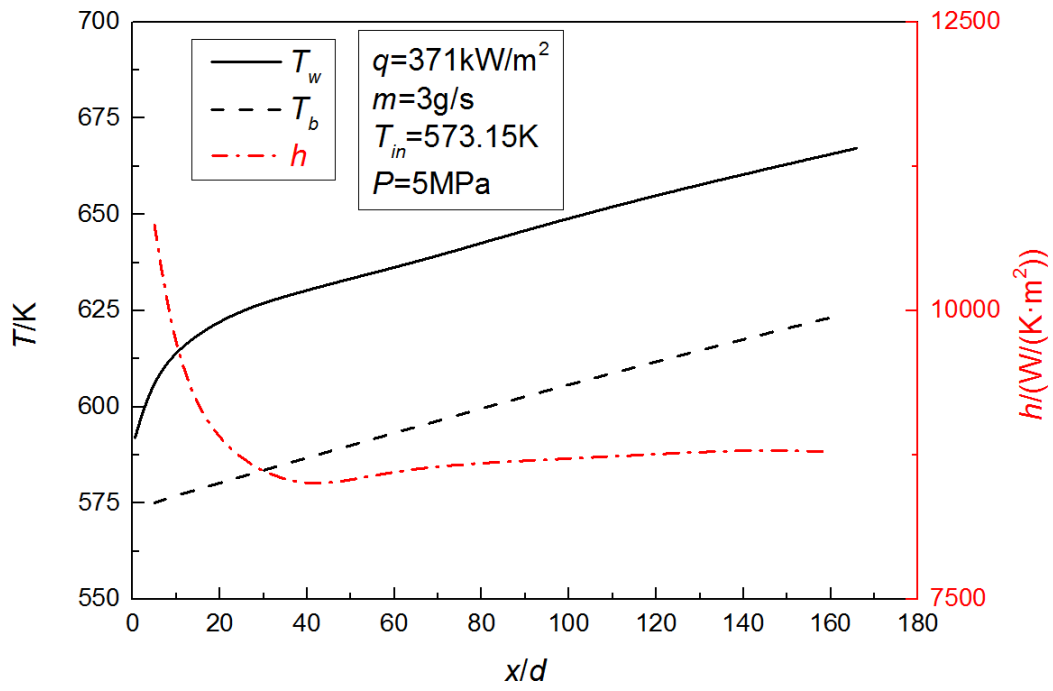
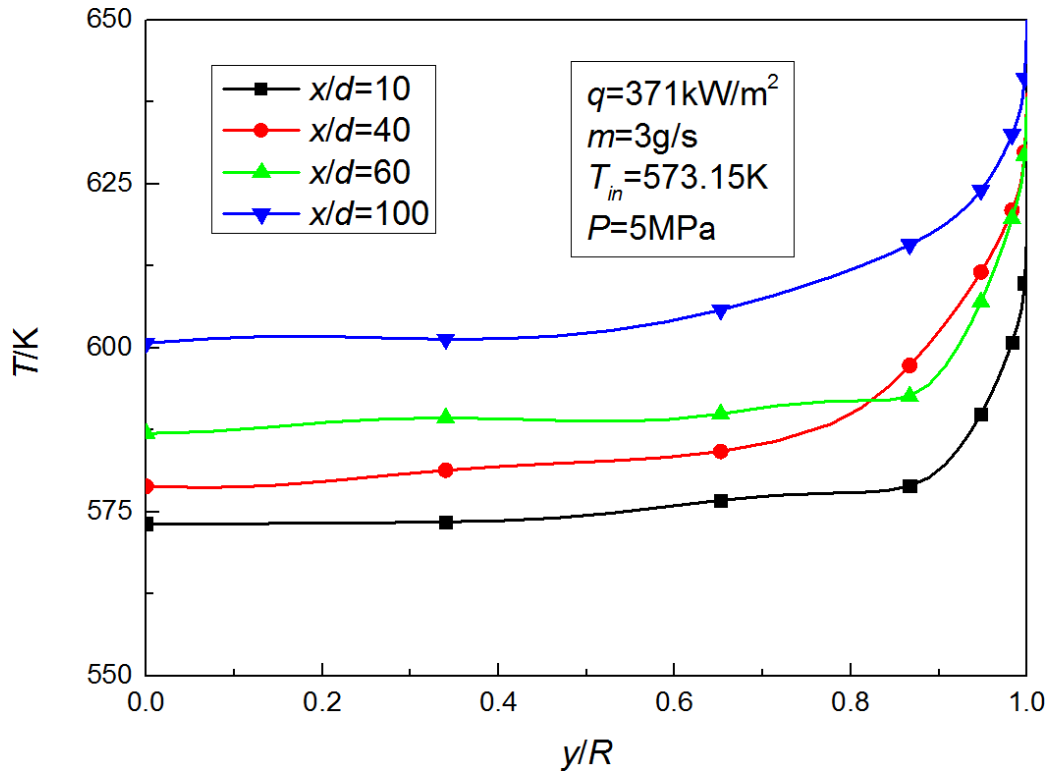
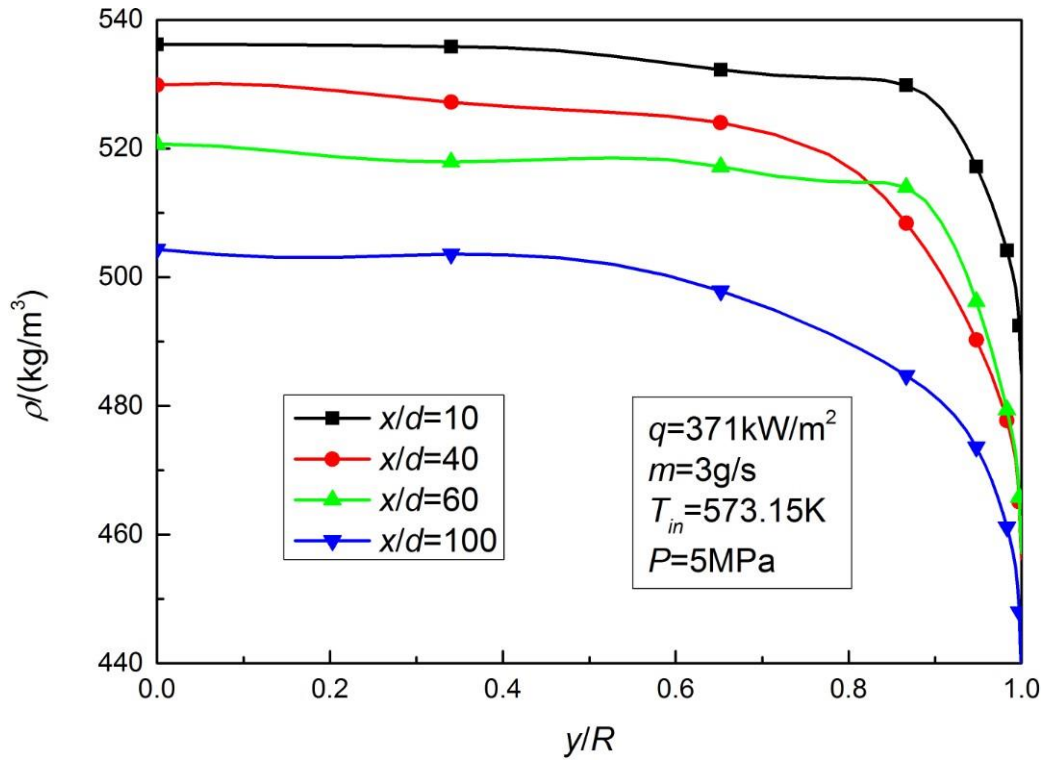


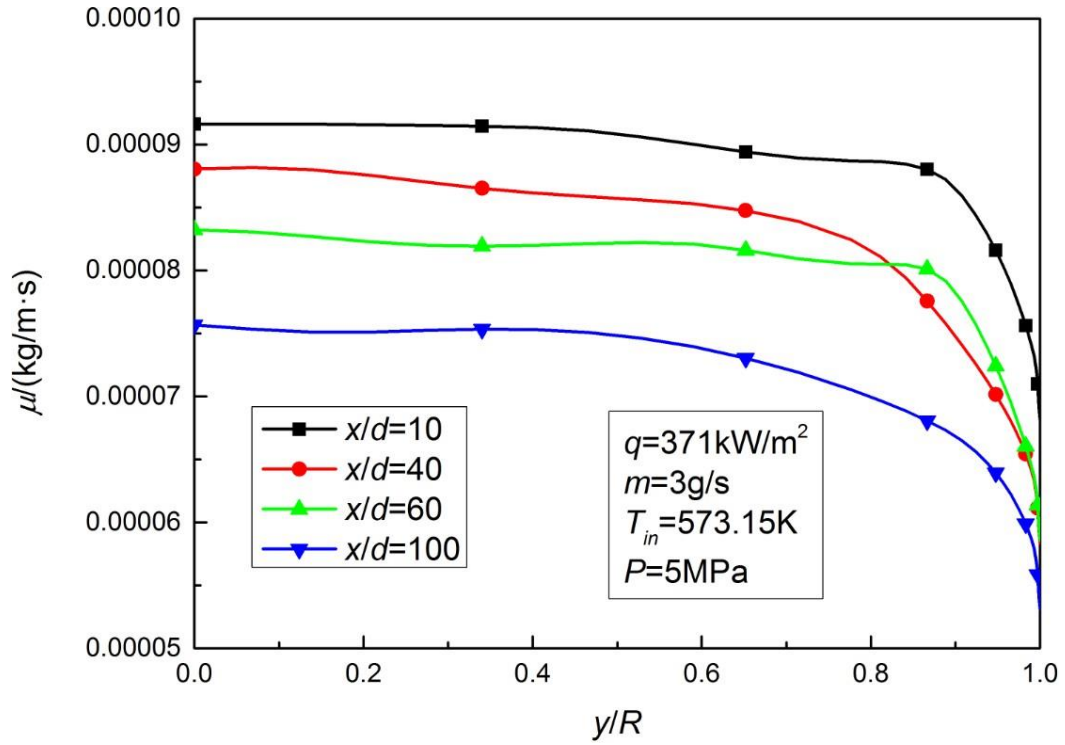
Fig. 17. Variations of the wall temperature, fluid bulk temperature and corresponding heat transfer coefficient with the non-dimensional distance by LES for case 3.



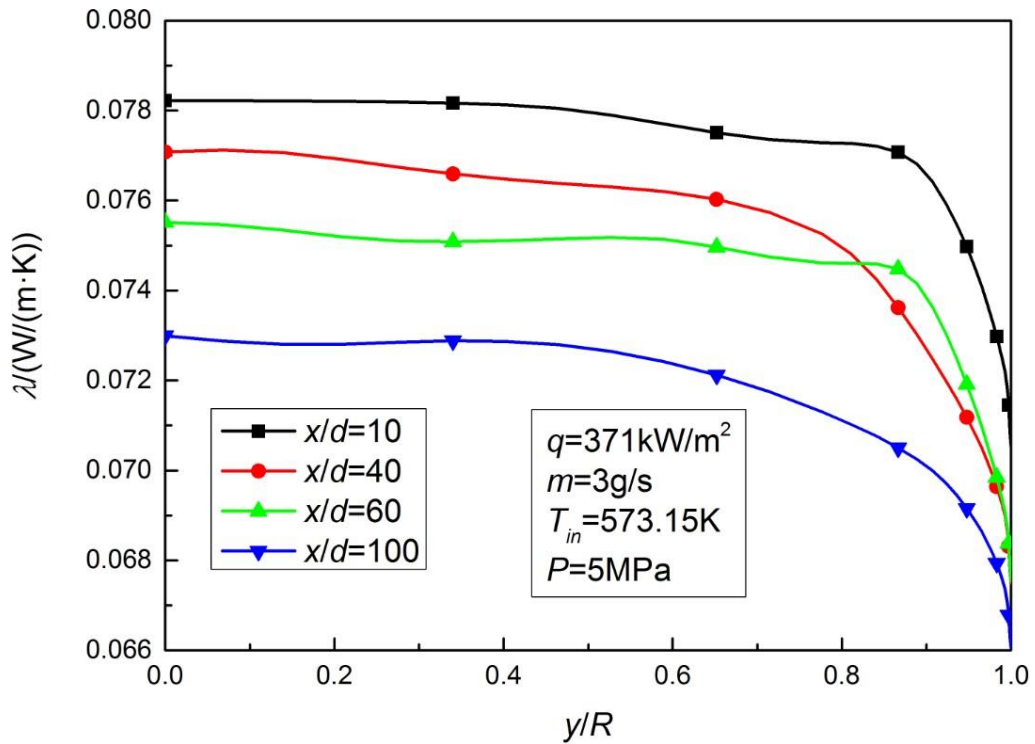
(a) Fluid temperature



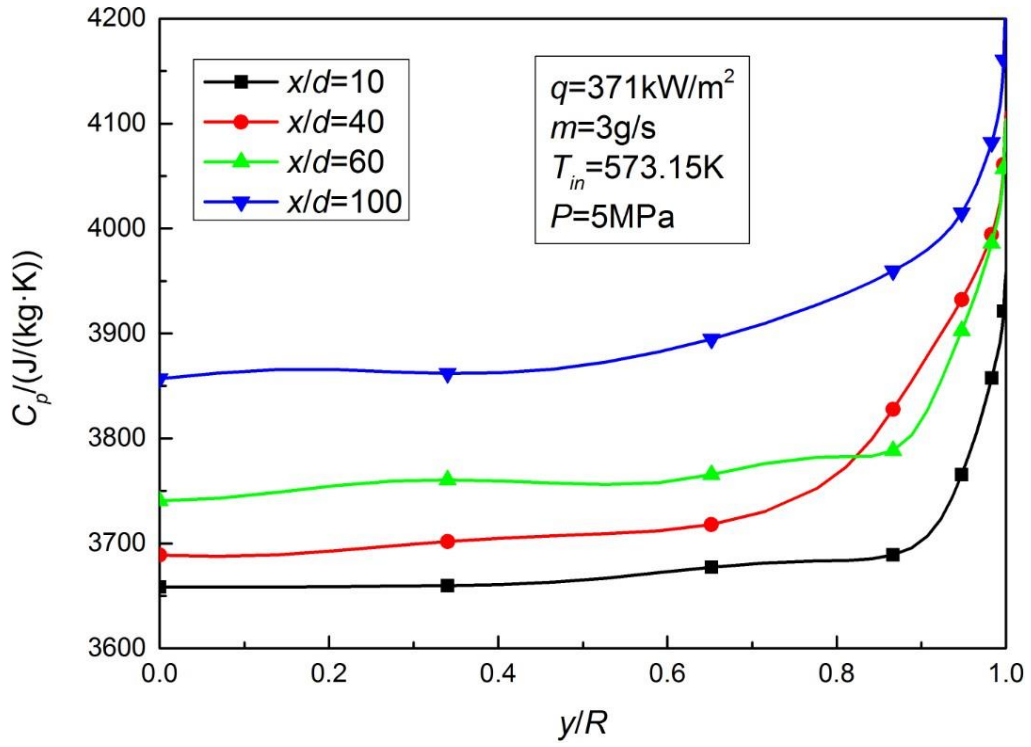
(b) Density



(c) Viscosity

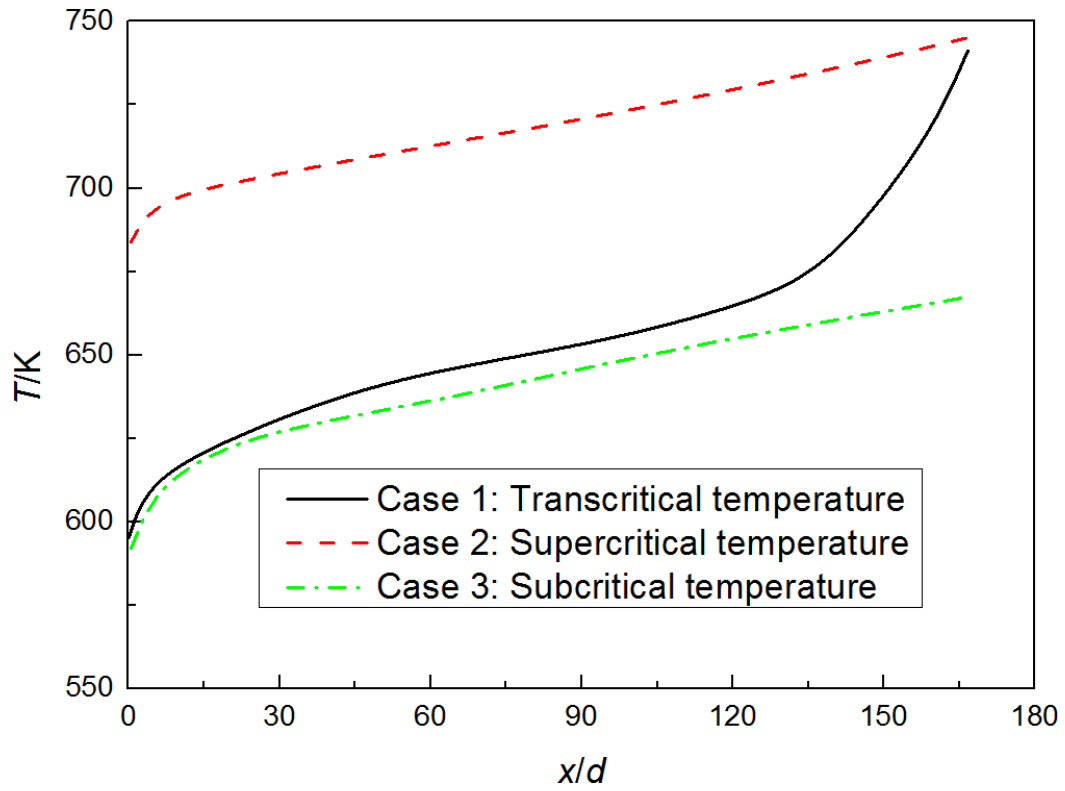


(d) Thermal conductivity

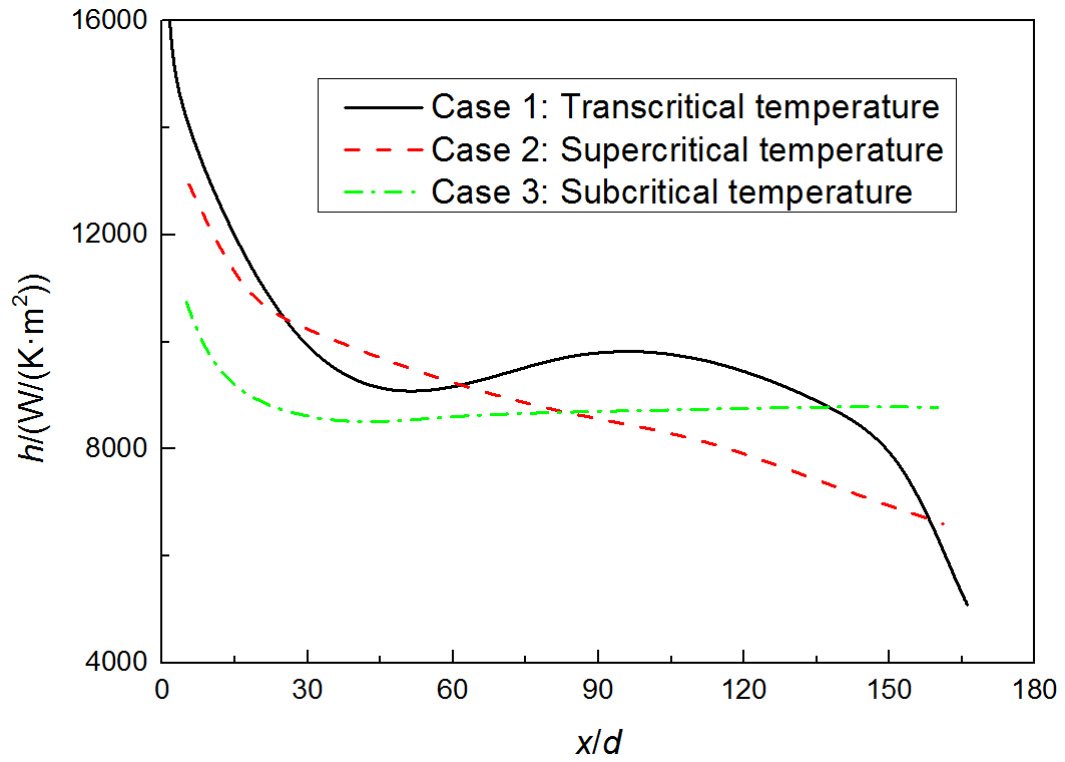


(e) Specific heat

Fig. 18. Radial variation of the fluid temperature and thermophysical properties at different axial locations along the pipe for case 3.



(a) Wall temperature



(b) Heat transfer coefficient

Fig. 19. Comparison of heat transfer characteristics for three cases.

Table 1 Grid resolution in the fluid domain.

Wall-normal y^+	Stream-wise Δx^+	Span-wise Δz^+
0.3	75	9

Table 2 Comparisons of relative errors of the total pressure drop along the tube length for three different cases.

Relative errors to the experimental results [31]			
	LES	SST $k-\omega$	LS $k-\varepsilon$
Case 1	-43.9%	-46.1%	-47.5%
Case 2	-35.9%	-57.4%	-58.9%
Case 3	-38.3%	-53.8%	-59.9%

